Relativistic many-body calculations of atomic properties in Pd-like ions[1]

U.I. Safronova, R. Bista, R. Bruch, and H. Merabet

Abstract: Wavelengths, transition rates, and line strengths are calculated for the 85 possible multipole transitions between the excited $4p^64d^94f$, $4p^64d^95l$, $4p^54d^{10}4f$, and $4p^54d^{10}5l$ states and the ground $4p^64d^{10}$ state in Pd-like ions with the nuclear charges ranging from $Z = 47$ to 100. Relativistic many-body perturbation theory (RMBPT), including the Breit interaction, is used to evaluate energies and transition rates for multipole transitions in hole–particle systems. This method is based on the relativistic many-body perturbation theory, agrees with MCDF calculations in lowest order, includes all second-order correlation corrections, and includes corrections from negative energy states. The calculations start from a [Zn]$4p^64d^{10}$ Dirac–Fock potential. First-order perturbation theory is used to obtain intermediate-coupling coefficients, and second-order RMBPT is used to determine the matrix elements. The contributions from negative-energy states are included in the second-order multipole matrix elements. The resulting transition energies and transition rates are compared with experimental values and with results from other recent calculations. Trends of the transitions rates for the selected multipole transitions as function of Z are illustrated graphically. The Z dependence of the energy splitting for all triplet terms of the $4p^64d^94f$ and $4p^64d^95l$ configurations are shown for $Z = 47$–100.

PACS Nos.: 31.15.Ar, 31.15.Md, 32.70.Cs, 32.30.Rj, 31.25.Jf

Résumé : Nous avons calculé les longueurs d'onde, les taux de transition et les intensités de ligne pour les 85 transitions multipolaires possibles entre les états excités $4p^64d^94f$,$4p^64d^95l$ et $4p^54d^{10}5l$ et le fondamental dans des ions de type Pd avec charge nucléaire $Z = 47$ à 100. Nous utilisons une théorie perturbative relativiste à N-corps (RMBPT), incluant une interaction de Breit, pour évaluer les énergies et les taux des transition multipolaires dans ces systèmes à particules–trous. Cette méthode est basée sur la théorie perturbative relativiste à N-corps ; elle agrée avec les calculs MCDF à l'ordre le plus bas et inclut toutes les corrections de corrélation au second ordre, ainsi que les corrections pour les états d'énergie négative. Les calculs débutent avec un potentiel de Dirac–Fock pour le [Zn]$4p^64d^{10}$. Nous utilisons d'abord la méthode perturbative au premier ordre pour calculer les coefficients de couplage intermédiaire et ensuite RMBPT au deuxième ordre pour déterminer les éléments de matrice. Les contributions venant des états d'énergie négative sont incluses dans les éléments de matrice multipolaire au second ordre. Nous comparons avec d'autres calculs nos résultats pour les énergies de transition et les taux de transition. Nous illustrons graphiquement en fonction de Z les tendances des taux de transition pour les multipoles sélectionnés. Nous donnons aussi les énergies de séparation pour tous les termes triplets des configurations $4p^64d^94f$ et $4p^64d^95l$ pour $Z = 47$ à 100.

[Traduit par la Rédaction]

1. Introduction

In the region of importance for extreme ultraviolet (EUV) lithography (near 134 Å) the strongest lines were identified as $4d^8$–$4d^75p$ transitions in Xe XI. The most intense lines in Xe IX were found to be the $4d^{10}\,{}^1S_0$–$4d^94f\,{}^1P_1$ line at 120.135 Å and the $4d^{10}\,{}^1S_0$–$4d^94f\,{}^3D_1$ line at 143.614 Å. Recent progress in the development of sources for EUV lithography was presented by O'Sullivan et al. in ref. 1. The emission of both Xe and Sn were investigated as sources for EUV lithography. To design extreme ultraviolet EUV sources for nanolithography, xenon EUV emission were studied experimentally in a plasma generated by the interaction of a high-power laser with a droplet jet [2]. Spectra from the Xe^{10+} ion were recorded at the National Institute of Standards and Technology (NIST) electron beam ion trap (EBIT) [3]. Experimental data on visible lines produced by Xe^{18+} to Xe^{35+} ions, obtained at the Lawrence Livermore National Laboratory (LLNL) EBIT were presented in ref. 4. At the Berlin EBIT facility, the 37 individual lines for Xe^{17+} to Xe^{25+} ions were registered in the range between 90 and 240 Å [5].

Atomic physics computations were performed using the Hebrew University Lawrence Atomic Code (HULLAC) to give a detailed account of the transitions involved. The importance of $4p$–$4d$, $4d$–$4f$, and $4d$–$5p$ transitions was stressed in ref. 2. Xenon spectra involving emission from ion species of Xe^{7+}

Received 8 March 2007. Accepted 4 June 2007. Published on the NRC Research Press Web site at http://cjp.nrc.ca/ on 5 February 2008.

U.I. Safronova,[2,3] R. Bista, and R. Bruch. Physics Department, University of Nevada, Reno, NV 89557, USA.
H. Merabet. College of Arts and Applied Sciences, Dhofar University, P.O. Box 2509, Salalah, Sultanate of Oman.

[1] Paper given at the Workshop on Twenty Years of Spectroscopy with EBIT held in Berkeley, California, 13–15 November 2006.
[2] Corresponding author (e-mail: ulyanas@unr.edu).
[3] On leave from ISAN, Troitsk, Russia.

 doi: 10.1139/P07-108 © 2008 NRC Canada

to Xe^{12+} were analyzed [6] for a plasma focus discharge developed for extreme ultraviolet lithography. Spectral analysis based on Hartree–Fock calculations showed that the $4d$–$5p$ transition arrays are fairly well-separated in wavelength for the ions Xe^{8+} to Xe^{11+} [6]. The generation of EUV light by a novel compact electron cyclotron resonance ion source (CECRIS) is studied in ref. 7. High-resolution spectra were recorded in the 10–16 nm range confirming significant contributions from highly excited Xe^{10+} and Xe^{9+} ionic states. Spectral analysis is based on Hartree–Fock calculations in ref. 7.

The importance of correlation and relativistic effects for the $4d$–$4f$ and $4d$–$5p$ electric-dipole transitions in Pd-like ions was investigated recently by Safronova et al. in ref. 8. Relativistic many-body perturbation theory (RMBPT) method is used in ref. 8 to evaluated excitation energies, line strengths, oscillator strengths, and transition probabilities in Pd-like ions with nuclear charges Z ranging from 49 to 100.

A detailed analysis of various transitions in Pd-like ions was performed by Churilov et al. [9–13]. To predict the $4d^{10}$–$4d^9(np + n'f)$ transitions in Cd III–Cs X, relativistic HF calculations using the Cowan code with scaling are carried out in ref. 9. The $4d^95l$–$4d^95l'$ spectra in Pd-like ions Sb VI, Te VII, and I VIII were investigated in the 400–900 Å region using vacuum spark sources as explained in ref. 10. Analysis of the spectra of Pd-like ions from Xe IX through Ce XIII is performed in ref. 11. Reference 12 gives the experimental results for the $4d^95s$, $4d^95d$, and $4d^95p$ states in Cs X–Ce XIII ions with the aid of high-resolution spectrographs supplemented by theoretical calculations carried out using the Cowan code and by fitting with orthogonal operator techniques. The spectra of palladium-like Pr^{13+} and Nd^{14+} ions excited in a laser-produced plasma source in the 70–700 Å region are investigated in ref. 13. Almost all the energy levels of the $4d^95s$, $4d^95p$, $4d^94f$, $4d^95d$, and $4d^95f$ configurations in Pr XIV and Nd XV were determined experimentally. The experimental level energies were described by Generalized Least Squares isoelectronic studies of $4d^95l$ configurations. It is emphasized in ref. 12 that ions of the palladium isoelectronic sequence are currently of interest for the development of X-ultraviolet (XUV) lasers.

The observation of XUV lasing at 41.81 nm on the $4d^95d\ ^1S_0$–$4d^95p\ ^1P_1$ transition in Pd-like Xe IX is reported by Lemoff et al. in ref. 14. In ref. 15, the authors confirm the classification in ref. 14 and adjust the energy level values involved in the laser scheme structure. One hundred and nine transitions were identified as combinations between levels of the $4d^95d$ with $4d^95p$ and $4d^95f$ configurations [15]. The energy parameters were obtained with Hartree–Fock relativistic calculations. Least-squares parametric calculation were carried out to study the fit between experimental and theoretical values [15]. The radiation from Pd-like W^{28+} in the extreme ultraviolet spectral region was investigated using a 2 m grazing-incidence spectrometer in conjunction with the Berlin EBIT [16]. The Pd-like W^{28+} spectra are among other tungsten spectra from W^{25+} to W^{36+} ions presented in ref. 16. An important part of the radiation emitted by these ions was observed in range 40–70 Å and was analyzed with the help of collisional-radiative line intensities using the HULLAC code [16].

The relative magnitudes of the electric-dipole (E1), the electric-quadrupole (E2), the electric-octupole (E3), the magnetic-dipole (M1), the magnetic-quadrupole (M2), and the magnetic-octupole (M3) radiative decay rates, calculated using the multiconfiguration DF approach, were presented in ref. 17 for the $4d^94f$, $4d^95s$, and $4d^95p$ states of Pd-like Yb^{24+}, Hg^{34+}, Th^{44+}, and U^{46+} ions.

In the present paper, RMBPT is used for the systematic study of the atomic characteristics of transitions in Pd-like ions with nuclear charge $Z = 47$–100. Specifically, we determine the energies of $4p^64d^94f(J)$, $4p^64d^95l(J)$, $4p^54d^104f(J)$, and $4p^54d^105l(J)$ states of Pd-like ions with nuclear charges $Z = 47$–100. The calculations are carried out to second order in perturbation theory. We consider the $4d$, $4p$ holes and the $4f$, $5s$, $5p$, $5d$, and $5f$ particles leading to the 68 odd-parity $4p^64d^94f(J)$, $4p^64d^95p(J)$, $4p^64d^95f(J)$, $4p^54d^105s(J)$, and $4p^54d^105d(J)$ excited states as well as the 56 even-parity $4p^64d^95s(J)$, $4p^64d^95d(J)$, $4p^54d^104f(J)$, $4p^54d^105p(J)$, and $4p^54d^105f(J)$, excited states in Pd-like ions with $Z = 47$ to 100. RMBPT is also used to determine line strengths, oscillator strengths, and transition rates for all allowed and forbidden electric-multipole and magnetic-multipole (E1, E2, E3, M1, M2, M3) transitions from $4p^64d^94f(J)$, $4p^64d^95l(J)$, $4p^54d^104f(J)$, and $4p^54d^105l(J)$ excited states to the ground state in Pd-like ions. Retarded E1, E2, and E3 matrix elements are evaluated in both length and velocity forms. A detailed discussion of the various contributions to the dipole matrix elements and energy levels is given for palladium-like xenon ($Z = 54$), which plays an important role in laser-produced plasma [2], Z-pinch plasma [18–20], gas-discharge plasma [21–26] for EUV lithography applications.

2. Method

Details of the RMBPT method are presented in ref. 27 for calculation of the energies of particle–particle states, in ref. 28 for calculation of energies of hole–particle states, in ref. 29 for calculation of radiative electric-dipole rates in two-particle states, in refs. 28 and 8 for calculation of radiative electric-dipole rates in hole–particle states, and in refs. 30–33 for calculation of radiative electric-dipole, electric-quadrupole, electric-octupole, magnetic-dipole, magnetic-quadrupole, and magnetic-octupole rates in Ne- and Ni-like systems. Here, we present only the model space for Pd-like ions without repeating the detailed discussions given in refs. 27–33. The calculations are carried out using sets of basis Dirac–Fock (DF) orbitals. The orbitals used in the present calculation are obtained as linear combinations of B-splines. These B-spline basis orbitals are determined using the method described in ref. 34. We use 50 B-splines of order 10 for each single-particle angular momentum state, and we include all orbitals with orbital angular momentum $l \leq 9$ in our basis set.

For atoms with one hole in closed shells and one electron above the closed shells, the model space is formed from hole–particle states of the type $a_v^+ a_a|0\rangle$ where $|0\rangle$ is the closed-shell $[Zn]4p_{1/2}^2 4p_{3/2}^4 4d_{3/2}^4 4d_{5/2}^6$ ground state, and a_i^+ and a_j are creation and annihilation operators, respectively. The single-particle indices v and a designate the valence and core states, respectively. For our study of low-lying states, $4l^{-1}nl'$ states of Pd-like ions, the values of a are $4p_{1/2}$, $4p_{3/2}$, $4d_{3/2}$, and $4d_{5/2}$, while the values of v are $4f_{5/2}$, $4f_{7/2}$, $5s_{1/2}$, $5p_{1/2}$, $5p_{3/2}$, $5d_{3/2}$, $5d_{5/2}$ $5f_{5/2}$, and $5f_{7/2}$.

In Fig. 1, we plot one-electron DF energies of the $4f_{7/2}$, $5s_{1/2}$, $5p_{3/2}$, $5d_{5/2}$, and $5f_{7/2}$ states as functions of Z. The $4f_{7/2}$ orbital is less tightly bound than the $5s_{1/2}$, $5p_{3/2}$, and $5d_{5/2}$

© 2008 NRC Canada

Table 1. Possible hole–particle states in the $4lj4fj'$ and $4lj5l'j'$ complexes; jj and LS coupling schemes.

Odd-parity states									
$J = 0, 5, 6$		$J = 1$		$J = 2$		$J = 3$		$J = 4$	
jj coupl.	LS coupl.	jj coupl.	LS coupl.	jj coupl.	LS coupl.	jj coupl.	LS coupl.	jj coupl.	LS coupl.
$4d_{3/2}5p_{3/2}(0)$	$4d5p\ ^3P_0$	$4d_{5/2}5p_{3/2}$	$4d5p\ ^3P$	$4d_{5/2}5p_{1/2}$	$4d5p\ ^3P$	$4d_{5/2}5p_{1/2}$	$4d5p\ ^3F$	$4d_{5/2}5p_{3/2}$	$4d5p\ ^3F$
$4d_{5/2}4f_{5/2}(0)$	$4d4f\ ^3P_0$	$4d_{3/2}5p_{1/2}$	$4d5p\ ^1P$	$4d_{5/2}5p_{3/2}$	$4d5p\ ^3F$	$4d_{5/2}5p_{3/2}$	$4d5p\ ^3D$	$4d_{5/2}4f_{5/2}$	$4d4f\ ^3H$
$4d_{5/2}5f_{5/2}(0)$	$4d5f\ ^3P_0$	$4d_{3/2}5p_{3/2}$	$4d5p\ ^3D$	$4d_{3/2}5p_{1/2}$	$4d5p\ ^1D$	$4d_{3/2}5p_{3/2}$	$4d5p\ ^1F$	$4d_{5/2}4f_{7/2}$	$4d4f\ ^3F$
$4p_{1/2}5s_{1/2}(0)$	$4p5s\ ^3P_0$	$4d_{5/2}4f_{5/2}$	$4d4f\ ^3P$	$4d_{3/2}5p_{3/2}$	$4d5p\ ^3D$	$4d_{5/2}4f_{5/2}$	$4d4f\ ^3F$	$4d_{3/2}4f_{5/2}$	$4d4f\ ^1G$
$4p_{3/2}5d_{3/2}(0)$	$4p5d\ ^3P_0$	$4d_{5/2}4f_{7/2}$	$4d4f\ ^3D$	$4d_{5/2}4f_{5/2}$	$4d4f\ ^3P$	$4d_{5/2}4f_{7/2}$	$4d4f\ ^3D$	$4d_{3/2}4f_{7/2}$	$4d4f\ ^3G$
$4d_{5/2}4f_{5/2}(5)$	$4d4f\ ^3H_5$	$4d_{3/2}4f_{5/2}$	$4d4f\ ^1P$	$4d_{5/2}4f_{7/2}$	$4d4f\ ^1D$	$4d_{3/2}4f_{5/2}$	$4d4f\ ^3G$	$4d_{5/2}5f_{5/2}$	$4d5f\ ^3F$
$4d_{5/2}4f_{7/2}(5)$	$4d4f\ ^1H_5$	$4d_{5/2}5f_{5/2}$	$4d5f\ ^3P$	$4d_{3/2}4f_{5/2}$	$4d4f\ ^3D$	$4d_{3/2}4f_{7/2}$	$4d4f\ ^1F$	$4d_{5/2}5f_{7/2}$	$4d5f\ ^1G$
$4d_{3/2}4f_{7/2}(5)$	$4d4f\ ^3G_5$	$4d_{5/2}5f_{7/2}$	$4d5f\ ^3D$	$4d_{3/2}4f_{7/2}$	$4d4f\ ^3F$	$4d_{5/2}5f_{5/2}$	$4d5f\ ^3F$	$4d_{3/2}5f_{5/2}$	$4d5f\ ^3H$
$4d_{5/2}5f_{5/2}(5)$	$4d5f\ ^3H_5$	$4d_{3/2}5f_{5/2}$	$4d5f\ ^1P$	$4d_{5/2}5f_{5/2}$	$4d5f\ ^3P$	$4d_{5/2}5f_{7/2}$	$4d5f\ ^1F$	$4d_{3/2}5f_{7/2}$	$4d5f\ ^3G$
$4d_{5/2}5f_{7/2}(5)$	$4d5f\ ^3G_5$	$4p_{3/2}5s_{1/2}$	$4p5s\ ^1P$	$4d_{5/2}5f_{7/2}$	$4d5f\ ^1D$	$4d_{3/2}5f_{5/2}$	$4d5f\ ^3D$	$4p_{3/2}5d_{5/2}$	$4p5d\ ^3F$
$4d_{3/2}5f_{7/2}(5)$	$4d5f\ ^1H_5$	$4p_{1/2}5s_{1/2}$	$4p5s\ ^3P$	$4d_{3/2}5f_{5/2}$	$4d5f\ ^3D$	$4d_{3/2}5f_{7/2}$	$4d5f\ ^3G$		
$4d_{5/2}4f_{7/2}(6)$	$4d4f\ ^3H_6$	$4p_{3/2}5d_{3/2}$	$4p5d\ ^3P$	$4d_{3/2}5f_{7/2}$	$4d5f\ ^3F$	$4p_{3/2}5d_{3/2}$	$4p5d\ ^3F$		
$4d_{5/2}5f_{7/2}(6)$	$4d5f\ ^3H_6$	$4p_{3/2}5d_{5/2}$	$4p5d\ ^1P$	$4p_{3/2}5s_{1/2}$	$4p5s\ ^3P$	$4p_{3/2}5d_{5/2}$	$4p5d\ ^3D$		
		$4p_{1/2}5d_{3/2}$	$4p5d\ ^3D$	$4p_{3/2}5d_{3/2}$	$4p5d\ ^3D$	$4p_{1/2}5d_{5/2}$	$4p5d\ ^3F$		
				$4p_{3/2}5d_{5/2}$	$4p5d\ ^1D$				
				$4p_{1/2}5d_{3/2}$	$4p5d\ ^3F$				
				$4p_{1/2}5d_{5/2}$	$4p5d\ ^3P$				

Even-parity states									
$J = 0, 5$		$J = 1$		$J = 2$		$J = 3$		$J = 4$	
jj coupl.	LS coupl.	jj coupl.	LS coupl.	jj coupl.	LS coupl.	jj coupl.	LS coupl.	jj coupl.	LS coupl.
$4d_{3/2}5d_{3/2}(0)$	$4d5d\ ^3P_0$	$4d_{3/2}5s_{1/2}$	$4d5s\ ^3D$	$4d_{5/2}5s_{1/2}$	$4d5s\ ^3D$	$4d_{5/2}5s_{1/2}$	$4d5s\ ^3D$	$4d_{5/2}5d_{3/2}$	$4d5d\ ^3G$
$4d_{5/2}5d_{5/2}(0)$	$4d5d\ ^1S_0$	$4d_{5/2}5d_{3/2}$	$4d5d\ ^3S$	$4d_{3/2}5s_{1/2}$	$4d5s\ ^1D$	$4d_{5/2}5d_{3/2}$	$4d5d\ ^3D$	$4d_{5/2}5d_{5/2}$	$4d5d\ ^3F$
$4p_{3/2}5p_{3/2}(0)$	$4p5p\ ^1S_0$	$4d_{5/2}5d_{5/2}$	$4d5d\ ^1P$	$4d_{5/2}5d_{3/2}$	$4d5d\ ^3D$	$4d_{5/2}5d_{5/2}$	$4d5d\ ^1F$	$4d_{3/2}5d_{5/2}$	$4d5d\ ^1G$
$4p_{1/2}5p_{1/2}(0)$	$4p5p\ ^3P_0$	$4d_{3/2}5d_{3/2}$	$4d5d\ ^3P$	$4d_{5/2}5d_{5/2}$	$4d5d\ ^3P$	$4d_{3/2}5d_{3/2}$	$4d5d\ ^3G$	$4p_{3/2}4f_{5/2}$	$4p4f\ ^3G$
$4d_{5/2}5d_{5/2}(5)$	$4d5d\ ^3G_5$	$4d_{3/2}5d_{5/2}$	$4d5d\ ^3D$	$4d_{3/2}5d_{3/2}$	$4d5d\ ^1D$	$4d_{3/2}5d_{5/2}$	$4d5d\ ^3F$	$4p_{3/2}4f_{7/2}$	$4p4f\ ^3F$
$4p_{3/2}4f_{7/2}(5)$	$4p4f\ ^3G_5$	$4p_{3/2}5p_{1/2}$	$4p5p\ ^3S$	$4d_{3/2}5d_{5/2}$	$4d5d\ ^3F$	$4p_{3/2}5p_{3/2}$	$4p5p\ ^3D$	$4p_{1/2}4f_{7/2}$	$4p4f\ ^1G$
$4p_{3/2}5f_{7/2}(5)$	$4p5f\ ^3G_5$	$4p_{3/2}5p_{3/2}$	$4p5p\ ^1P$	$4p_{3/2}5p_{1/2}$	$4p5p\ ^3D$	$4p_{3/2}4f_{5/2}$	$4p4f\ ^3D$	$4p_{3/2}5f_{5/2}$	$4p5f\ ^3G$
		$4p_{1/2}5p_{1/2}$	$4p5p\ ^3D$	$4p_{3/2}5p_{3/2}$	$4p5p\ ^3P$	$4p_{3/2}4f_{7/2}$	$4p4f\ ^1F$	$4p_{3/2}5f_{7/2}$	$4p5f\ ^3F$
		$4p_{1/2}5p_{3/2}$	$4p5p\ ^3P$	$4p_{1/2}5p_{3/2}$	$4p5p\ ^3D$	$4p_{1/2}4f_{5/2}$	$4p4f\ ^3G$	$4p_{1/2}5f_{7/2}$	$4p5f\ ^3G$
		$4p_{3/2}4f_{5/2}$	$4p4f\ ^3D$	$4p_{3/2}4f_{5/2}$	$4p4f\ ^3D$	$4p_{1/2}4f_{7/2}$	$4p4f\ ^3D$		
		$4p_{3/2}5f_{5/2}$	$4p5f\ ^3D$	$4p_{3/2}4f_{7/2}$	$4p4f\ ^1D$	$4p_{3/2}5f_{5/2}$	$4p5f\ ^3D$		
				$4p_{1/2}4f_{5/2}$	$4p4f\ ^1D$	$4p_{3/2}5f_{7/2}$	$4p5f\ ^1F$		
				$4p_{3/2}5f_{5/2}$	$4p5f\ ^3D$	$4p_{1/2}5f_{5/2}$	$4p5f\ ^3G$		
				$4p_{3/2}5f_{7/2}$	$4p5f\ ^1D$	$4p_{1/2}5f_{7/2}$	$4p5f\ ^3D$		
				$4p_{1/2}5f_{5/2}$	$4p5f\ ^3F$				

© 2008 NRC Canada

Fig. 1. One-electron Dirac–Fock energies ($E/(Z-35)^2$ in cm^{-1}) of $4f_j$ and $5l_j$ states as functions of Z.

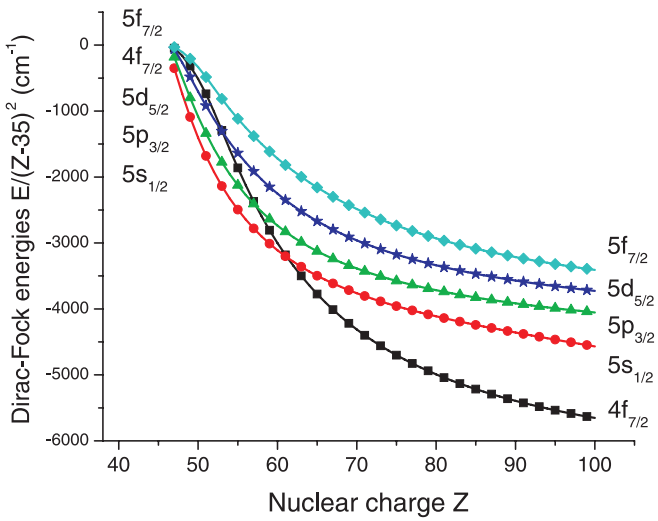

Fig. 2. Second-order one-particle contributions to the energies (a.u.) as functions of Z.

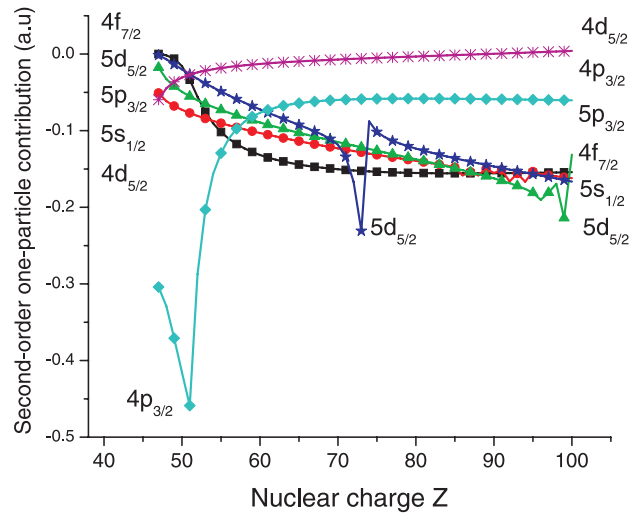

orbitals at low stages of ionization, while $4f$ orbitals are more tightly bound than the $5d$, $5p$, and $5s$ orbitals for ions with $Z =$ 54, 58, and 62, respectively. Competition between the $4f$ and $5d$, $5p$, and $5s$ orbitals leads to problems for RMBPT, making it difficult to obtain very accurate excitation energies and line strengths for the transition between the low-lying $4d^94f$ and $4d^95l$ excited states and the ground state. Collapse of the $4f$ orbital for Xe-like ions was investigated by O'Sullivan [35] and Cheng and Froese-Fischer [36].

To obtain orthonormal model states, we consider the coupled states $\Phi_{JM}(av)$ defined by

$$\Phi_{JM}(av) = \sqrt{(2J+1)} \sum_{m_a m_v} (-1)^{j_v - m_v} \times \left(j_v \quad J \quad j_a - m_v \quad M \quad m_a\right) a^{\dagger}_{vm_v} a_{am_a} |0\rangle \quad (1)$$

Combining the $4p_j, 4d_j$ hole orbitals and the $4f_j, 5s_j, 5p_j, 5d_j$, $5f_j$ particle orbitals, we obtain 68 odd-parity states consisting of 5 $J = 0$ states, 14 $J = 1$ states, 17 $J = 2$ states, 14 $J = 3$ states, 10 $J = 4$ states, six $J = 5$ states, and two $J = 6$ states. Additionally, there are 56 even-parity states consisting of 4 $J = 0$ states, 11 $J = 1$ states, 15 $J = 2$ states, 14 $J = 3$ states, 9 $J = 4$ states, and three $J = 5$ states. The distribution of the 124 states in the model space is summarized in Table 1. In Table 1, we give both jj and LS designations for hole–particle states. Instead of using the $4l_j^{-1}nl'_{j'}$ or $4l^{-1}nl'$ designations, we use simpler designations $4l_jnl'_{j'}$ or $4lnl'$ in this table and in all the following tables and the text below.

3. Excitation energies

3.1. Example: Energy matrix for Xe^{8+}

In Table 2, we give the various contributions to the second-order energies for the special case of Pd-like xenon, $Z = 54$. In Table 2, we show the one-body and two-body second-order Coulomb contributions to the energy matrix labeled $E_1^{(2)}$ and $E_2^{(2)}$, respectively. The corresponding Breit–Coulomb contributions are given in columns headed $B_1^{(2)}$ and $B_2^{(2)}$ of Table 2. The one-body second-order energy is obtained as a sum of the valence $E_v^{(2)}$ and hole $E_a^{(2)}$ energies with the latter being the dominant contribution. The second-order one-particle $E_v^{(2)}$ and one-hole $E_a^{(2)}$ contributions are defined by three terms: double sums, single sums, and a one-potential term (see eq. (2.7) in ref. 28). The second-order two-body contribution $E_2^{(2)}$ is defined by four terms: double sums, single sums, random-phase approximation (RPA), and one-potential terms (see eqs. (2.8)–(2.11) in ref. 28). All of the expressions in ref. 28 were defined for the Coulomb interaction. When we include the Breit interaction in the calculation, the Coulomb matrix element Xk(ab,cd) is exchanged by magnetic radial integrals Mk(ab,cd) and Nk(ab,cd) defined by eqs. (A4) and (A5) in ref. 37.

The values of $E_1^{(2)}$ and $B_1^{(2)}$ are nonzero only for diagonal matrix elements. Although there are 124 diagonal and 1494 nondiagonal matrix elements for the $4l_j4f_{j'}(J)$ and $4l_j5l'_{j'}(J)$ hole–particle states, we list only the part of even-parity subset with $J = 2$ in Table 2. The second-order Breit–Coulomb corrections are relatively large and, therefore, must be included in accurate calculations. The values of nondiagonal matrix elements given in columns headed $E_2^{(2)}$ and $B_2^{(2)}$ are comparable with values of diagonal two-body matrix elements. However, the values of one-body contributions, $E_1^{(2)}$ and $B_1^{(2)}$, are larger than the values of two-body contributions, $E_2^{(2)}$ and $B_2^{(2)}$, respectively. As a result, total second-order diagonal matrix elements are much larger than the nondiagonal matrix elements, which are shown in Table 2.

In Fig. 2, we illustrate the Z dependence of the second-order hole ($4p$, $4d$) energies $E_a^{(2)}$ and valence ($4f$, $5s$, $5p$, $5d$) energies $E_v^{(2)}$ in Pd-like ions. As we see from Fig. 2, $E_v^{(2)}$ slowly increases with Z for valence contributions; however, the $E_a^{(2)}$ decreases with Z for hole contributions. The value of $E_a^{(2}$ for the $4p$ hole state is very large for low-Z ions. The importance of the including of the $4p^54d^{10}nl$ states in the basis set of orbitals for atomic structure Cowan code was underlined by Churilov et al. in refs. 10–13. We observe several sharp features in the curves describing the $5d_{5/2}$ state ($Z = 74$) and the $4p_{3/2}$ state

© 2008 NRC Canada

Table 2. Second-order contributions to the energy matrices (a.u.) for even-parity states with $J = 2$ in the case of Pd-like xenon, $Z = 54$. One- and two-body second-order Coulomb and Breit–Coulomb contributions are given in columns labeled $E_1^{(2)}$, $E_2^{(2)}$, $B_1^{(2)}$, and $B_2^{(2)}$, respectively.

		Coulomb interaction		Breit–Coulomb corr.	
$4l_1j_1\ nl_2j_2$,	$4l_3j_3\ nl_4j_4$	$E_1^{(2)}$	$E_2^{(2)}$	$B_1^{(2)}$	$B_2^{(2)}$
$4d_{5/2}5s_{1/2}$	$4d_{5/2}5s_{1/2}$	−0.108864	0.030810	0.009448	0.000592
$4d_{5/2}5d_{5/2}$	$4d_{5/2}5d_{5/2}$	−0.063417	0.000720	0.010656	0.000310
$4p_{3/2}5p_{3/2}$	$4p_{3/2}5p_{3/2}$	−0.225446	0.013871	0.011761	0.000506
$4p_{3/2}4f_{5/2}$	$4p_{3/2}4f_{5/2}$	−0.248315	0.076271	0.008905	0.000810
$4p_{3/2}5f_{5/2}$	$4p_{3/2}5f_{5/2}$	−0.190703	0.011807	0.012376	−0.000136
$4d_{3/2}5s_{1/2}$	$4d_{3/2}5d_{5/2}$	0.000000	−0.002403	0.000000	0.000002
$4d_{3/2}5d_{5/2}$	$4d_{3/2}5s_{1/2}$	0.000000	−0.000354	0.000000	−0.000015
$4d_{5/2}5s_{1/2}$	$4p_{3/2}5p_{1/2}$	0.000000	−0.035357	0.000000	−0.000045
$4p_{3/2}5p_{1/2}$	$4d_{5/2}5s_{1/2}$	0.000000	−0.144028	0.000000	0.000173

Table 3. Contributions to the energy matrix $E[4l_1j_1\ nl_2j_2, 4l_3j_3\ nl_4j_4] = E^{(0)} + E^{(1)} + E^{(2)} + B_{hf}^{(1)} + B^{(2)}$ before diagonalization. These contributions are given for a hole–particle ion with a [Zn]$4p^64d^{10}$ core, in the case of even-parity states with $J = 2$, and $Z = 54$.

$4l_1j_1\ nl_2j_2$,	$4l_3j_3\ nl_4j_4$	$E^{(0)}$	$E^{(1)}$	$B_{hf}^{(1)}$	$E^{(2)}$	$B^{(2)}$
$4d_{5/2}5s_{1/2}$	$4d_{5/2}5s_{1/2}$	2.782935	−0.643533	−0.003992	−0.076987	0.009894
$4d_{5/2}5d_{5/2}$	$4d_{5/2}5d_{5/2}$	4.177776	−0.503341	−0.006092	−0.062698	0.010967
$4p_{3/2}5p_{3/2}$	$4p_{3/2}5p_{3/2}$	6.752066	−0.584162	−0.012683	−0.211574	0.012268
$4p_{3/2}4f_{5/2}$	$4p_{3/2}4f_{5/2}$	7.368658	−0.820717	−0.013878	−0.172043	0.009715
$4p_{3/2}5f_{5/2}$	$4p_{3/2}5f_{5/2}$	8.377342	−0.431353	−0.014818	−0.178896	0.012240
$4d_{3/2}5s_{1/2}$	$4d_{3/2}5d_{5/2}$	0.000000	0.022143	0.000007	−0.002403	0.000002
$4d_{3/2}5d_{5/2}$	$4d_{3/2}5s_{1/2}$	0.000000	0.022143	0.000007	−0.000354	−0.000015
$4d_{5/2}5s_{1/2}$	$4p_{3/2}5p_{1/2}$	0.000000	−0.030205	−0.000009	0.005336	0.000020
$4p_{3/2}5p_{1/2}$	$4d_{5/2}5s_{1/2}$	0.000000	−0.030205	−0.000009	0.021929	−0.000016

($Z = 51$). The origin of these singularities is associated with the fact that the $n = 4$ shell is not filled in Pd-like ions; such singularities are not present in the one-electron spectra of Li-like, Na-like, or Cu-like ions, where the $n = 1$, $n = 2$, and $n = 3$ shells, respectively, are filled. These singularities occur when the $4d^{10}5d_j$ levels cross excited even-parity levels of the $4d^94f^2$ configuration. At all such crossings, energy denominators in the expression for $E^{(2)}$ vanish and the perturbation expansion fails. To remove these irregularities, it would be necessary to base the perturbative treatment on a lowest order wave function that includes both one-particle and two-particle one-hole states, a treatment that is beyond the scope of the present paper. Away from these crossings, the perturbation expansion works well, as seen by the close agreement of our results with available experimental data.

In Table 3, we present results for the zeroth-, first-, and second-order Coulomb contributions, $E^{(0)}$, $E^{(1)}$, and $E^{(2)}$, and the first- and second-order Breit–Coulomb corrections, $B_{hf}^{(1)}$ and $B^{(2)}$. The importance of the correlation contribution is evident from Table 3; the ratio of the first and zeroth orders ($E^{(1)}/E^{(0)}$) is about 5–20%, and the ratio of the second and first ($E^{(2)}/E^{(1)}$) orders is even larger, 15–40%. It should be noted that corrections for the frequency-dependent Breit interaction [37] are included in the first order only. The difference between the first-order Breit corrections calculated with and without frequency dependence is 1–3%, however, the ratio of the first-order Breit and Coulomb corrections is also 1–3%. As one can see from Table 3, the ratio of nondiagonal and diagonal matrix elements is larger for the first-order contributions than for the second-order contributions. Another difference in the first- and second-order contributions is the symmetry properties: the first-order nondiagonal matrix elements are symmetric, but the second-order nondiagonal matrix elements are not symmetric. The values of $E^{(2)}[a'v'(J), av(J)]$ and $E^{(2)}[av(J), a'v'(J)]$ matrix elements differ in some cases by a factor 2–3 and occasionally have opposite signs.

We now discuss how the final energy levels are obtained from the above contributions. To determine the first-order energies of the states under consideration, we diagonalize the symmetric first-order effective Hamiltonian, including both the Coulomb and Breit interactions. The first-order expansion coefficient $C^N[av(J)]$ (often called a mixing coefficient) is the Nth eigenvector of the first-order effective Hamiltonian, and $E^{(1)}[N]$ is the corresponding eigenvalue. The resulting eigenvectors are used to determine the second-order Coulomb correction $E^{(2)}[N]$, the second-order Breit–Coulomb correction $B^{(2)}[N]$, and the quantum electrodynamic (QED) correction $E_{\mathrm{Lamb}}[N]$.

© 2008 NRC Canada

Table 4. Energies of Pd-like xenon for even-parity states with $J = 2$ relative to the ground state. $E^{(0+1)} \equiv E^{(0)} + E^{(1)} + B^{(1)}_{hf}$.

jj coupl.	LS coupl.	$E^{(0+1)}$	$E^{(2)}$	$B^{(2)}$	E_{LAMB}	E_{tot}
$4d_{5/2}5s_{1/2}$	$4d5s\ ^3D_2$	2.12839	−0.08004	0.00990	0.00339	2.06163
$4d_{3/2}5s_{1/2}$	$4d5s\ ^1D_2$	2.20532	−0.07135	0.01004	0.00384	2.14786
$4d_{5/2}5d_{3/2}$	$4d5d\ ^3D_2$	3.64080	−0.06063	0.01104	−0.00030	3.59090
$4d_{5/2}5d_{5/2}$	$4d5d\ ^3P_2$	3.66926	−0.05903	0.01097	−0.00021	3.62099
$4d_{3/2}5d_{3/2}$	$4d5d\ ^1D_2$	3.73810	−0.06420	0.01113	0.00023	3.68525
$4d_{3/2}5d_{5/2}$	$4d5d\ ^3F_2$	3.74327	−0.06332	0.01113	0.00024	3.69131
$4p_{3/2}5p_{1/2}$	$4p5p\ ^3D_2$	6.04308	−0.20703	0.01241	−0.00120	5.84725
$4p_{3/2}5p_{3/2}$	$4p5p\ ^3P_2$	6.15826	−0.21462	0.01229	−0.00092	5.95501
$4p_{1/2}5p_{3/2}$	$4p5p\ ^3D_2$	6.44057	−0.19842	0.00973	−0.00115	6.25074
$4p_{3/2}4f_{5/2}$	$4p4f\ ^3D_2$	6.59410	−0.19505	0.01169	−0.00040	6.41034
$4p_{3/2}4f_{7/2}$	$4p4f\ ^1D_2$	6.62545	−0.17095	0.01152	−0.00059	6.46542
$4p_{1/2}4f_{5/2}$	$4p4f\ ^1D_2$	7.03397	−0.27274	0.01081	−0.00020	6.77184
$4p_{3/2}5f_{5/2}$	$4p5f\ ^3D_2$	7.94759	−0.19762	0.01232	0.00115	7.76344
$4p_{3/2}5f_{7/2}$	$4p5f\ ^1D_2$	7.97193	−0.19119	0.01228	0.00117	7.79419
$4p_{1/2}5f_{5/2}$	$4p5f\ ^3F_2$	8.43004	−0.22252	0.01340	0.00011	8.22104

Fig. 3. Mixing coefficients for the $4d5d\,^3D_1$ and $4d5s\,^3D_2$ levels as functions of Z. $Q = 4d5d\,^3D_1$ and $Q = 4d5s\,^3D_2$ for the left and right panels of the figure, respectively.

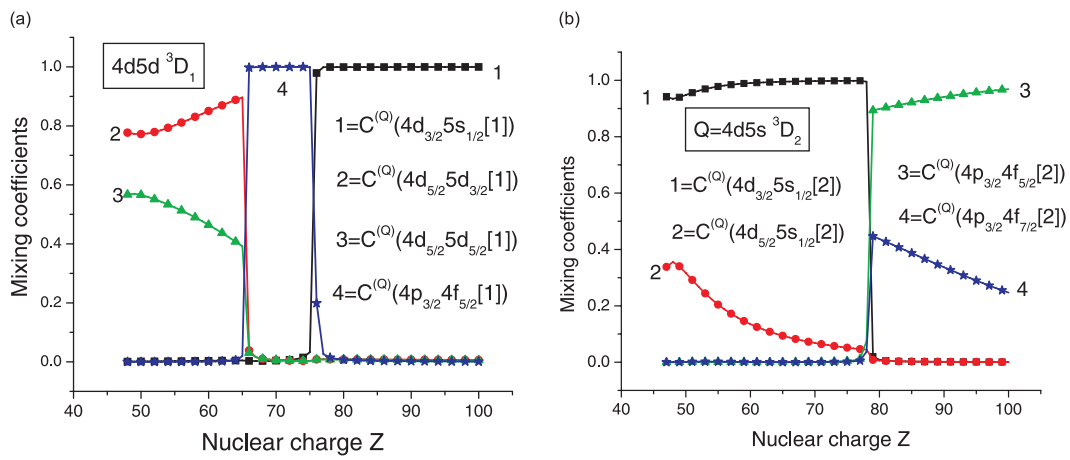

Fig. 4. Energies $E/(Z-35)^2$ in cm^{-1} for the even- and odd-parity states in Pd-like ions shown on the left and right panels of the figure, respectively.

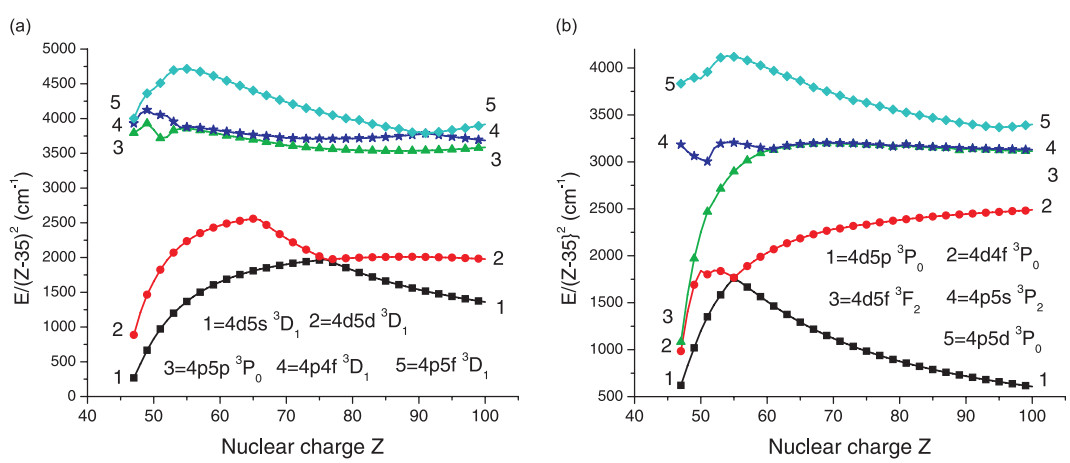

© 2008 NRC Canada

In Table 4, we list the following contributions to the energies of 13 excited states in Xe^{8+}: the sum of the zeroth- and first-order energies $E^{(0+1)} = E^{(0)} + E^{(1)} + B^{(1)}_{hf}$, the second-order Coulomb energy $E^{(2)}$, the second-order Breit–Coulomb correction $B^{(2)}$, the QED correction $E_{\rm LAMB}$, and the sum of the above contributions $E_{\rm tot}$. The QED correction is approximated as the sum of the one-electron self energy and the first-order vacuum-polarization energy. The screened self-energy and vacuum polarization data given by Kim et al. [38], which are in close agreement with the screened self-energy calculations by Blundell [39], are used to determine the QED correction $E_{\rm LAMB}$.

When starting calculations from relativistic DF wave functions, it is natural to use jj designations for uncoupled energy matrix elements; however, neither jj nor LS coupling describes the *physical* states properly, except for the single-configuration state $4d_{5/2}4g_{9/2}(7) \equiv 4d4g\ ^3I_7$. Both designations are used in Table 4. We have already mentioned the importance of including the correlation contribution to obtain accurate energy values for Pd-like ions. The second-order Coulomb contribution $E^{(2)}$ gives 2–3% to the total values of energies in the case of Xe^{8+} ion (compare the values with headings $E^{(2)}$ and $E^{(0)}$ in Table 4).

3.2. *Z*-dependence of eigenvectors and eigenvalues in Pd-like ions

In Figs. 3 and 4, we illustrate the Z-dependence of the eigenvectors and eigenvalues of the $4d_j\ 4f_{j'}\ (J)$ and $4l_j\ 5l'_{j'}\ (J)$ hole–particle states. We refer to a set of states of the same parity and the same J as a complex of states. Strong mixing of the $4d_j\ 4f_{j'}\ (1)$ and $4d_j\ 5p_{j'}\ (1)$ hole–particle states is discussed in ref. 8. For even-parity complex with $J = 1$ and 2, we found strong mixing for states with $4p$ and $4d$ holes, i.e., $4d_j5s_{1/2}\ (J)$ and $4p_j\ 4f_{j'}\ (J)$ states. In Fig. 3, we show the dependence of the eigenvectors using the example of even-parity states with $J = 1$ and $J = 2$. This particular $J = 1$ even-parity complex includes 11 states that are listed in Table 1. Using the first-order expansion coefficients $C^N[av(J)]$ defined in the previous section, we can present the resulting eigenvectors as

$$\begin{aligned}\Phi(N) = {} & C^N[4d_{3/2}5s_{1/2}(1)]\Phi[4d_{3/2}5s_{1/2}(1)] \\ & + C^N[4d_{5/2}5d_{3/2}(1)]\Phi[4d_{5/2}5d_{3/2}(1)] + C^N[4d_{5/2}5d_{5/2}(1)]\Phi[4d_{5/2}5d_{5/2}(1)] \\ & + C^N[4d_{3/2}5d_{3/2}(1)]\Phi[3d_{3/2}5d_{3/2}(1)] + C^N[4d_{3/2}5d_{5/2}(1)]\Phi[4d_{3/2}5d_{5/2}(1)] \\ & + C^N[4p_{3/2}5p_{1/2}(1)]\Phi[4p_{3/2}5p_{1/2}(1)] + C^N[4p_{3/2}5p_{3/2}(1)]\Phi[4p_{3/2}5p_{3/2}(1)] \\ & + C^N[4p_{1/2}5p_{1/2}(1)]\Phi[4p_{1/2}5p_{1/2}(1)] + C^N[4p_{1/2}5p_{3/2}(1)]\Phi[4p_{1/2}5p_{3/2}(1)] \\ & + C^N[4p_{3/2}4f_{5/2}(1)]\Phi[4p_{3/2}4f_{5/2}(1)] + C^N[4p_{3/2}5f_{5/2}(1)]\Phi[4p_{3/2}5f_{5/2}(1)] \qquad (2)\end{aligned}$$

As a result, 121 $C^N[av(J)]$ coefficients are needed to describe the 11 eigenvalues. For simplicity, we plot only four of the 11 mixing coefficients for the level $N = 4d5d\ ^3D_1$ in the left panel of Fig. 3. These coefficients are chosen to illustrate the mixing of the states; the remaining mixing coefficients give very small contributions to this level. We observe strong mixing between $[4d_{5/2}5d_j(1)]+[4p_{3/2}4f_{5/2}(1)]$ states for $Z = 65-66$ and $[4d_{3/2}5s_{1/2}(1)]+[4p_{3/2}4f_{5/2}(1)]$ states for $Z = 75-76$. We plot four of the 15 mixing coefficients for the $N = 4d5s\ ^3D_2$ level in the right panel of Fig. 3. The mixing of the $[4d_{3/2}5s_{1/2}(2)]+[4p_{3/2}4f_{5/2}(1)]$ states leads to the sharp feature in the region of $Z = 78$–79.

Energies, relative to the ground state, of even- and odd-parity states with $J = 0$, 1, and 2, divided by $(Z - 35)^2$, are shown in Fig. 4. It should be noted that the $(Z - 35)^2$ factor was introduced to provide better presentation of the energy diagrams. We plot the limited number of energy levels to illustrate Z dependence choosing one representative from a configuration. As a result, we show 5 levels from 68 odd-parity states, and 5 levels from 56 even-parity states in Fig. 4. We find that $E/(Z-35)^2$ slowly increases with Z for the most of levels, except for the $4d5s\ ^3D_1$ and $4d5p\ ^3P_0$ levels. The curve describing the energy of the $4d5s\ ^3D_1$ level almost crosses the energy of the $4d5d\ ^3D_1$ level. The difference in energies between two levels is equal to 40 cm^{-1} at $Z = 76$ (about 0.001% from energy of these levels). It is known that the crossing of energy levels inside the one complex with fixed J is forbidden by the Wigner and Neumann theorem (see, for example, ref. 40).

We can observe from the left panel of Fig. 4 that the curves describing the energy of the $4d5s\ ^3D_1$ and $4d5d\ ^3D_1$ levels does not cross at at $Z = 76$ and curve 2 stays above curve 1 for the entire range $Z = 47$–100. The similar behavior of the curves describing the energy of the $4d5p\ ^3P_0$ and $4d4f\ ^3P_0$ levels is seen on the right panel of Fig. 4. The difference in energies for these levels at $Z = 55$ is equal to 2519 cm^{-1}, that is about 0.3% from energy of these levels. The energy of the $4d5f\ ^3F_2$ level increases very rapidly with Z and becomes almost equal to the energy of the $4p5s\ ^3P_2$ level for $Z \geq 60$ (see curves 3 and 4 on the right panel of Fig. 4).

The energy differences between levels of odd- and even-parity triplet terms, divided by $(Z - 35)^2$, are illustrated in Fig. 5. The energy-splitting intervals for the triplet terms shown in Fig. 5 are smaller than the excitation energies shown in Fig. 4 by a factor of 50–100. As a result, the influence of the correlation and relativistic effects becomes more evident for the splitting of terms. We observe a very sharp change of splitting with Z for all curves shown in Fig. 5, while the Z dependencies of curves demonstrated by Fig. 4 are rather smooth. The sharp feature at $Z = 55$–56 illustrated in Fig. 5 for the splitting of the $4d5p\ ^3P_J$ and $4d5p\ ^3F_J$ terms is caused by strong mixing between $4p5d$ and $4d4f$ configurations that is discussed in ref. 8. The mixing of the $[4d_{3/2}5s_{1/2}(2)] + [4p_{3/2}4f_{5/2}(1)]$ states exhibits the sharp feature in the region of $Z = 78$–79 for the $4d5s\ ^3D_J$ splittings shown on the right bottom

© 2008 NRC Canada

panel of Fig. 5. Our calculations show that the fine structures of almost all levels illustrated in Fig. 5 do not follow the Landé rules even for small Z. The unusual splittings may be caused by changes from LS to jj coupling, with mixing from other triplet and singlet states. The different J states are mixed differently. Further experimental confirmation would be very helpful in verifying the correctness of these sometimes sensitive mixing parameters.

4. Electric-dipole, electric-quadrupole, and electric-octupole matrix elements

We calculate electric-dipole (E1) matrix elements for the transitions between the 14 odd-parity $4d_j5p_{j'}(1)$, $4d_j4f_{j'}(1)$, $4d_j5f_{j'}(1)$, $4p_j5s_{1/2}(1)$, and $4p_j5d_{j'}(1)$ excited states and the ground state, electric-octupole (E3) matrix elements between the 15 even-parity $4d_j5s_{1/2}(2)$, $4d_j5d_{j'}(2)$, $4p_j5p_{j'}(2)$, $4p_j4f_{j'}(2)$, and $4p_j5f_{j'}(2)$ excited states and the ground state, and electric-quadrupole (E2) matrix elements between the 14 odd-parity $4d_j5p_{j'}(3)$, $4d_j4f_{j'}(3)$, $4d_j5f_{j'}(3)$, and $4p_j5d_{j'}(3)$ excited states and the ground state for Pd-like ions with nuclear charges $Z = 47$–100.

The first- and second-order Coulomb corrections and second-order Breit–Coulomb corrections to reduced E1 and E2 matrix elements will be referred to as $Z^{(1)}$, $Z^{(2)}$, and $B^{(2)}$, respectively, throughout the text. These contributions are calculated in both length and velocity gauges. In this section, we show the importance of different contributions and discuss the gauge dependence of the E1, E2, and E3 matrix elements.

The evaluation of the first- and second-order reduced multipole matrix elements — Coulomb: $Z^{(1)}$, $Z^{(2)}$, and Breit: $B^{(2)}$, — for palladium-like ions follows the pattern of the corresponding calculation for nickel-like ions ref. 28. The second-order reduced matrix element $Z^{(2)}$ for the transition between the hole–particle states and the ground state consists of three contributions: Dirac–Hartree–Fock (HF) term ($Z^{(\mathrm{HF})}$), RPA term ($Z^{(\mathrm{RPA})}$), and the derivative (derv) term, $Z^{(\mathrm{derv})}$. Analytical expressions of the first-order $Z^{(1)}$ and the second-order contributions $Z^{(\mathrm{DF})}$, $Z^{(\mathrm{RPA})}$, and $Z^{(\mathrm{derv})}$ for transitions between excited ground state in hole–particle systems are given by eqs. (2.13)–(2.16) in ref. 28. The K-pole matrix elements $Z^{(1)}$, that include retardation, are given by eqs. (38, 39) of ref. 41 and Appendix A of ref. 31.

4.1. Example: E1, E2, and E3 matrix elements for Xe^{8+}

In Table 5, we list values of *uncoupled* first- and second-order E1, E2, and E3 matrix elements $Z^{(1)}$, $Z^{(2)}$, $B^{(2)}$, together with derivative terms $P^{(\mathrm{derv})}$, for Pd-like xenon, $Z = 54$ (for details, see, refs. 31–33). We list values for the E1 transitions between odd-parity states with $J = 1$ and the ground state, the E2 transitions between even-parity states with $J = 2$ and the ground state, and the E3 transitions between odd-parity states with $J = 3$ and the ground state. Matrix elements in both length (L) and velocity (V) forms are given. We can see that the first-order matrix elements, $Z_L^{(1)}$ and $Z_V^{(1)}$, differ by 15–20%; however, the L–V differences between second-order matrix elements are much larger for some transitions. For the E1 transitions, the derivative term in length form, $P_L^{(\mathrm{derv})}$, is almost equal to $Z_L^{(1)}$, but the derivative term in velocity form, $P_V^{(\mathrm{derv})}$, is smaller than $Z_V^{(1)}$ by three to four orders of magnitude. For the E2 transitions, the value of $P^{(\mathrm{derv})}$ in velocity form almost equals $Z^{(1)}$ in velocity form, and the $P^{(\mathrm{derv})}$ in length form is larger than $Z^{(1)}$ in length form by a factor of two. For the E3 transitions, the value of $P^{(\mathrm{derv})}$ in velocity form is larger than $Z^{(1)}$ in velocity form by a factor of two, and the $P^{(\mathrm{derv})}$ in length form is larger than $Z^{(1)}$ in length form by factor of three.

Values of E1, E2, and E3 *coupled* reduced matrix elements in length and velocity forms are illustrated in Table 6 for the limited set of transitions. Although we use an intermediate-coupling scheme, it is nevertheless convenient to label the physical states using the jj labelling for high-Z and the LS labelling for low-Z; both designations are used in Table 6. The first two columns in Table 6 show L and V values of *coupled* reduced matrix elements calculated in first order. The $L - V$ difference is about 15–20%. Including the second-order contributions (columns headed RMBPT in Table 6) decreases the $L - V$ difference to 1–5%. This $L - V$ difference arises because we start our RMBPT calculations using a nonlocal Dirac–Fock (DF) potential. If we were to replace the DF potential by a local potential, the differences would disappear completely. It should be emphasized that we include the negative energy state (NES) contributions to sums over intermediate states (see ref. 29 for details).

4.2. Z-dependences of E1, E2, and E3 matrix elements in Pd-like ions

In Fig. 6, differences between length (L) and velocity (V) forms are illustrated for the various contributions to uncoupled $0 - 4d_{3/2}5p_{1/2}(1)$, $0 - 4d_{5/2}5d_{3/2}(2)$, and $0 - 4d_{5/2}5p_{1/2}(3)$ matrix elements, where 0 is the ground state. We observe that the curves describing the first-order matrix elements $Z_L^{(1)}$ and $Z_V^{(1)}$ smoothly decrease with Z; however, the curves describing the second-order matrix elements $Z_L^{(2)}$, $B_L^{(2)}$, $Z_V^{(2)}$, and $B_V^{(2)}$ have deep minima. The differences between $Z_L^{(1)}$ and $Z_V^{(1)}$ decrease with Z and are equal to 25–35% for $Z = 50$ and 9–12% for $Z = 70$. In the case of E1 transitions, the ratio of the second-order contributions $Z_L^{(2)}$ and $Z_V^{(2)}$ is equal to 2.5 for $Z = 50$ and decreases with increasing Z to 0.13 for $Z = 70$. The value of the second-order Coulomb matrix elements $Z_L^{(2)}$ becomes smaller than the value of the second-order Breit matrix elements $B_L^{(2)}$ and $B_V^{(2)}$ at $Z = 65$ and $Z = 66$, respectively. Similar behavior is found for the curves describing the second-order octupole (E3) matrix elements (see bottom panel of Fig. 6). The second-order Coulomb matrix elements $0 - 4d_{5/2}5p_{1/2}(3)$ in length form, $Z_L^{(2)}$, become smaller than all other three second-order matrix elements $B_L^{(2)}$, $Z_V^{(2)}$, and $B_V^{(2)}$ at $Z \geq 70$.

The difference between length- and velocity-forms for E2 transitions is illustrated in the top right panel of Fig. 6 for the uncoupled $0 - 4d_{5/2}5d_{3/2}(2)$ matrix element. In the case of E2 transitions, the difference between $Z_L^{(1)}$ and $Z_V^{(1)}$ decreases with Z to 8% for high-Z ions. The difference between $Z_L^{(2)}$ and $Z_V^{(2)}$ increases with increasing Z from 8% for $Z = 50$ to 25% for $Z \geq 70$. The difference between $B_L^{(2)}$ and $B_V^{(2)}$ is very large, but the values of the second-order Breit matrix elements $B_L^{(2)}$ and $B_V^{(2)}$ are smaller than the values of the second-order Coulomb matrix elements $Z_L^{(2)}$ and $Z_V^{(2)}$ for the uncoupled $0 - 4d_{5/2}5d_{3/2}(2)$ matrix element.

© 2008 NRC Canada

Fig. 5. Energy splitting ($\Delta E/(Z-35)^2$ in cm^{-1}) for terms of odd- and even-parity states in Pd-like ions as function of Z.

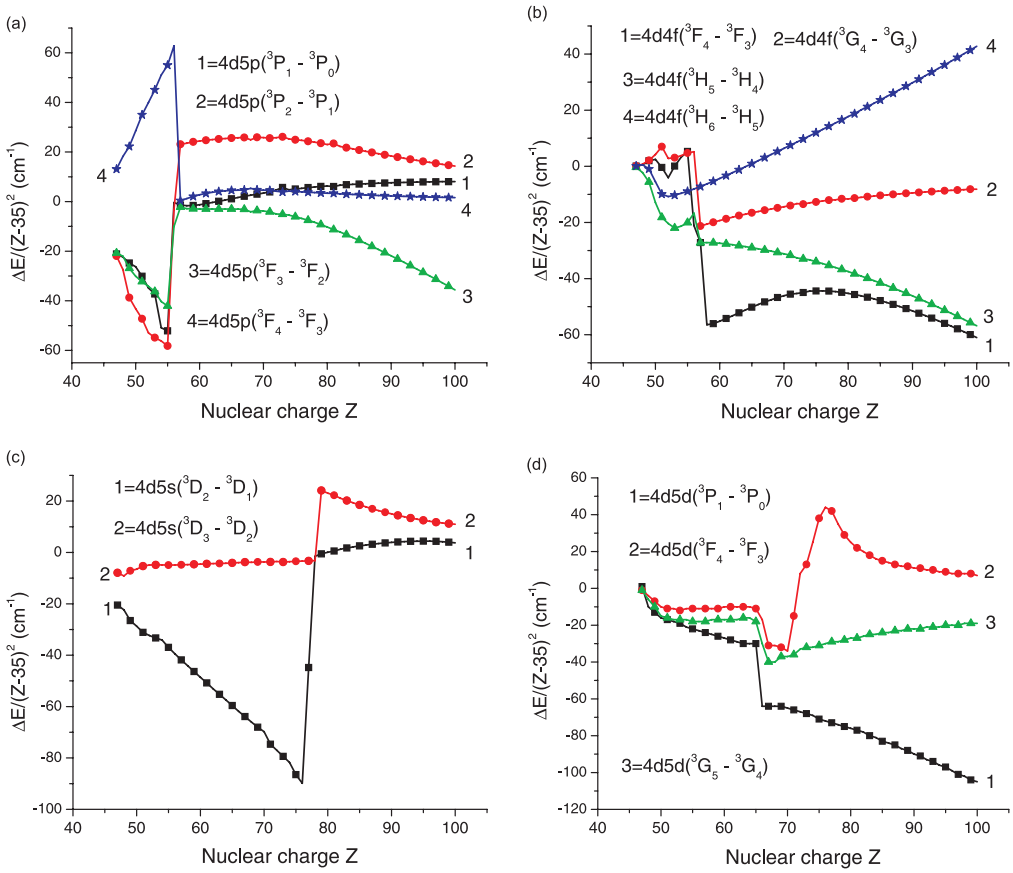

Table 5. E1, E2, and E3 uncoupled reduced matrix elements in length L and velocity V forms for transitions from $av(J)$ states with $J = 1$, 2, and 3 into the ground state in Xe^{8+}.

$av(J)$	$Z_L^{(1)}$	$Z_V^{(1)}$	$Z_L^{(2)}$	$Z_V^{(2)}$	$B_L^{(2)}$	$B_V^{(2)}$	$P_L^{(\mathrm{derv})}$	$P_V^{(\mathrm{derv})}$
E1 uncoupled reduced matrix elements								
$4d_{5/2}5p_{3/2}(1)$	−0.60237	−0.45923	0.00200	−0.02531	0.00001	0.00086	−0.60225	−0.00006
$4d_{5/2}4f_{7/2}(1)$	1.58706	1.23617	−0.23568	0.08026	0.00111	−0.00131	1.58649	−0.00062
$4d_{5/2}5f_{7/2}(1)$	0.38190	0.28900	−0.07140	0.03354	0.00022	−0.00038	0.38189	−0.00012
$4p_{3/2}5s_{1/2}(1)$	−0.31860	−0.25472	0.02022	0.00003	−0.00043	0.00024	−0.31839	0.00001
$4p_{3/2}5d_{5/2}(1)$	0.06338	0.05135	0.04517	0.01580	0.00032	0.00021	0.06307	−0.00015
E2 uncoupled reduced matrix elements								
$4d_{5/2}5s_{1/2}(2)$	−0.90058	−0.65040	0.01094	−0.00867	−0.00124	0.00002	−1.80112	−0.65050
$4d_{5/2}5d_{5/2}(2)$	0.60153	0.49652	0.05947	0.06505	0.00087	0.00010	1.20280	0.49638
$4p_{3/2}5p_{1/2}(2)$	0.35847	0.29250	0.24127	0.22223	0.00072	0.00014	0.71674	0.29249
$4p_{3/2}4f_{7/2}(2)$	−1.07218	−0.88408	−0.83482	−0.79029	−0.00147	0.00048	−2.14349	−0.88316
$4p_{3/2}5f_{7/2}(2)$	−0.26953	−0.21817	−0.36515	−0.33318	−0.00013	0.00036	−0.53901	−0.21802
E3 uncoupled reduced matrix elements								
$4d_{5/2}5p_{3/2}(3)$	1.05857	0.83941	0.00753	0.02213	0.00203	0.00074	3.18866	1.67878
$4d_{3/2}4f_{5/2}(3)$	−1.09763	−0.89164	0.05569	0.09700	−0.00307	−0.00094	−3.28816	−1.78313
$4d_{5/2}5f_{7/2}(3)$	0.21652	0.22152	0.11274	0.11943	0.00070	0.00051	0.65126	0.44277
$4p_{3/2}5d_{3/2}(3)$	0.44858	0.38218	0.12640	0.12996	0.00127	0.00050	1.35238	0.76422

The differences between results in length and velocity forms shown in Fig. 6 are compensated by additional second-order terms called "derivative terms" $P^{(\mathrm{derv})}$; they are defined by eq. (2.16) of ref. 28 (see, also Tables 5 and 6). The derivative terms arise because transition amplitudes depend on the energy, and the transition energy changes order-by-order in RMBPT calculations.

© 2008 NRC Canada

Table 6. E1, E2, and E3 coupled reduced matrix elements in length L and velocity V forms for transitions from $av(J)$ states into the ground state in Xe^{8+}.

		First order		RMBPT	
$av(J)$	$av(LSJ)$	L	V	L	V
E1 coupled reduced matrix elements					
$4d_{3/2}5p_{1/2}(1)$	$4d5p\ ^1P_1$	−0.71612	−0.54649	−0.70907	−0.70267
$4d_{3/2}4f_{5/2}(1)$	$4d4f\ ^1P_1$	1.96130	1.53122	1.67641	1.64343
$4d_{5/2}5f_{7/2}(1)$	$4d5f\ ^3D_1$	0.22181	0.17013	0.18741	0.18013
$4p_{3/2}5s_{1/2}(1)$	$4p5s\ ^1P_1$	0.28398	0.22801	0.27669	0.27125
$4p_{1/2}5d_{3/2}(1)$	$4p5d\ ^3D_1$	0.03323	0.02642	−0.01625	−0.01650
E2 coupled reduced matrix elements					
$4d_{3/2}5s_{1/2}(2)$	$4d5s\ ^1D_2$	0.90870	0.66357	0.61578	0.68005
$4d_{5/2}5d_{5/2}(2)$	$4d5d\ ^3P_2$	0.60861	0.50279	0.58822	0.59015
$4d_{3/2}5d_{3/2}(2)$	$4d5d\ ^1D_2$	−0.62091	−0.51446	−0.58196	−0.58612
$4p_{3/2}4f_{5/2}(2)$	$4p4f\ ^3D_2$	−0.73965	−0.60926	−0.75248	−0.74633
E3 coupled reduced matrix elements					
$4d_{5/2}5f_{7/2}(3)$	$4d5f\ ^1F_3$	−0.07875	−0.07274	−0.11884	−0.11094
$4d_{3/2}5f_{7/2}(3)$	$4d5f\ ^3G_3$	0.09254	0.08519	0.14804	0.14846
$4p_{3/2}5d_{3/2}(3)$	$4p5d\ ^3F_3$	0.48884	0.41740	0.65150	0.65491
$4p_{3/2}5d_{5/2}(3)$	$4p5d\ ^3D_3$	0.22116	0.18688	0.39485	0.38310

Fig. 6. The first- and second-order Coulomb corrections ($Z^{(1)}$, $Z^{(2)}$), and second-order Breit–Coulomb corrections ($B^{(2)}$) for E1, E2, and E3 uncoupled matrix elements for transitions between excited and ground states calculated in length (L) and velocity (V) forms in Pd-like ions.

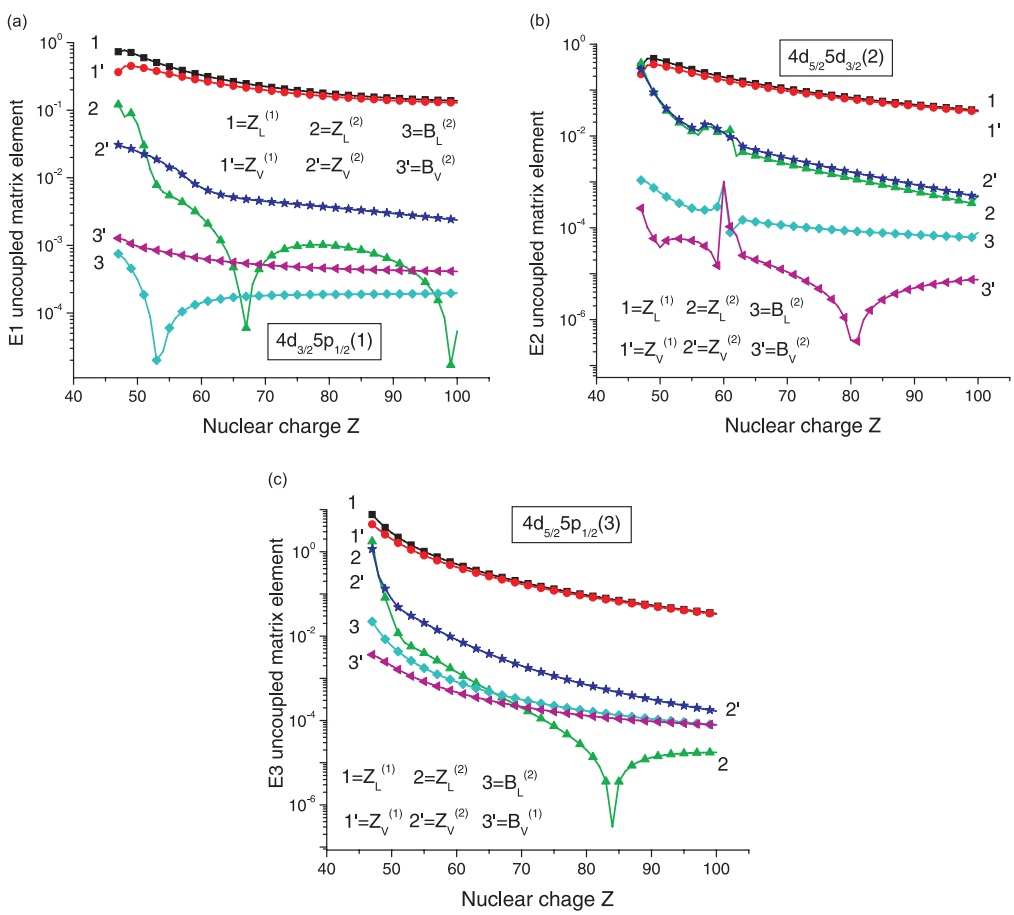

© 2008 NRC Canada

Fig. 7. The first- and second-order corrections ($Z^{(1)}$, $Z^{(2)}$) for M1, M2, and M3 uncoupled matrix elements for transition between excited and ground states in Pd-like ions. The first-order ($Z^{(1)}$) matrix elements calculated in nonrelativistic ($Z^{(1)}_{\mathrm{NR}}$), relativistic frequency-independent($Z^{(1)}_{\mathrm{R}}$), and relativistic frequency-dependent ($Z^{(1)}_{\mathrm{RF}}$) approximations are presented. The second-order Coulomb ($Z^{(2)}_{\mathrm{CL}}$) and Breit–Coulomb corrections ($Z^{(2)}_{\mathrm{BR}}$) are also given.

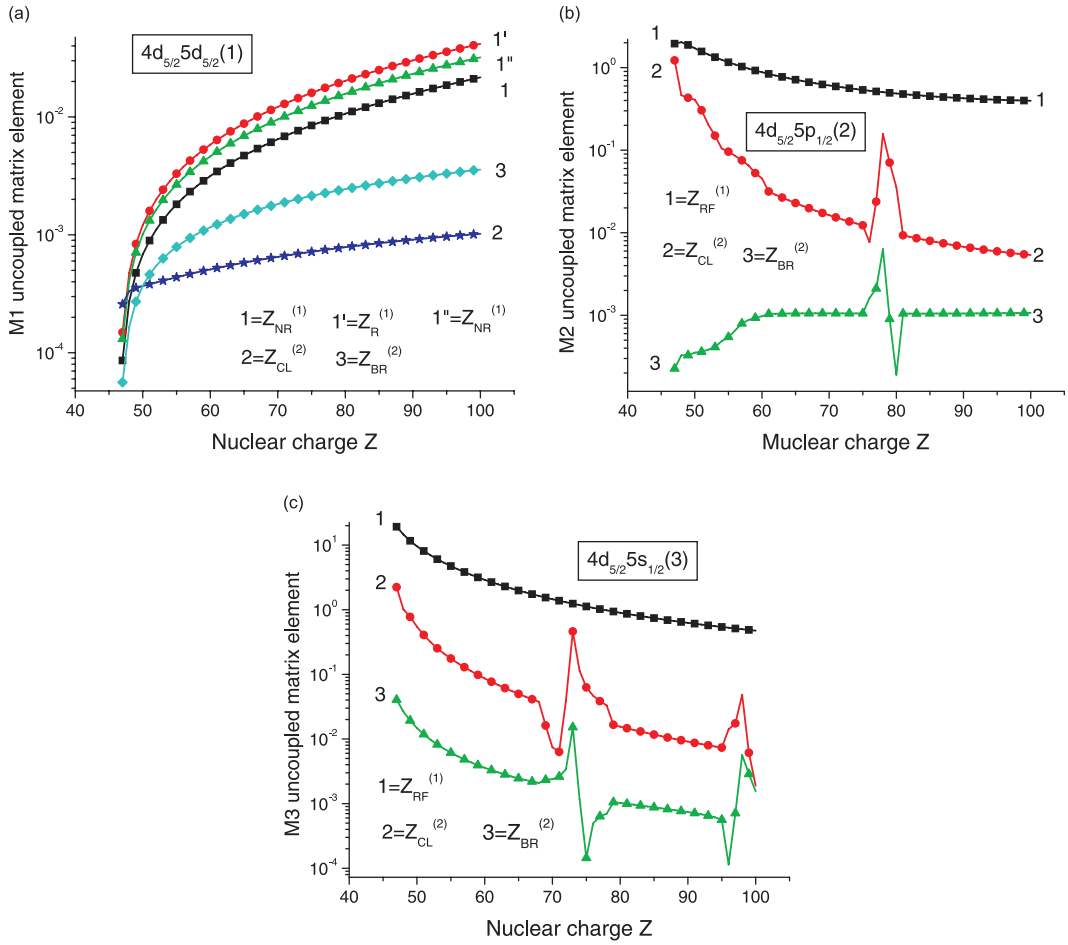

Fig. 8. The total M1 line strengths ($S^{(1+2)}_{\mathrm{RF}}$) between the $4d5s\ ^3D_1$ excited state and the ground state in Pd-like ions as function of Z. The first-order ($S^{(1)}$) line strengths calculated in nonrelativistic ($S^{(1)}_{\mathrm{NR}}$), relativistic frequency-independent ($S^{(1)}_{\mathrm{R}}$), and relativistic frequency-dependent approximations ($S^{(1)}_{\mathrm{RF}}$) are presented.

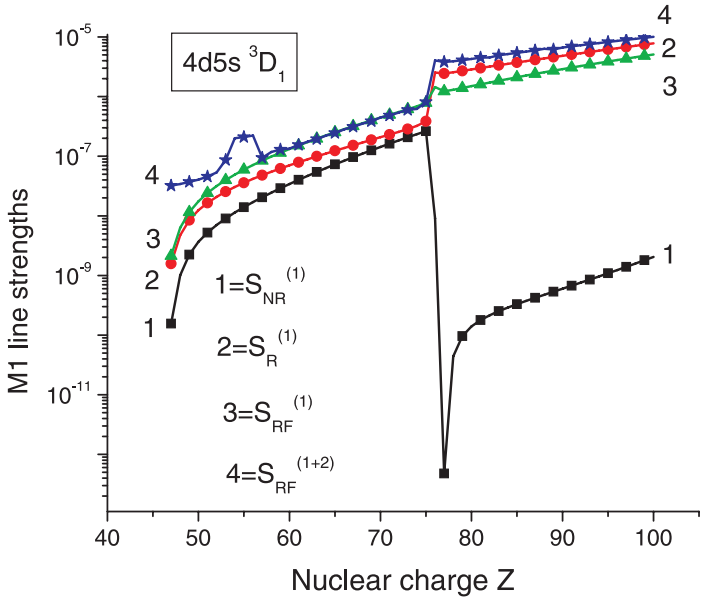

© 2008 NRC Canada

Table 7. Energies (10^3cm^{-1}) of odd- and even-parity states relative to the ground state in Pd-like xenon. Comparison of the RMBPT data and data from the COWAN code [43] with experimental values [11].

Level	RMBPT	Expt.	COWAN	Level	RMBPT	Expt.	COWAN
$4d_{3/2}5s_{1/2}\ ^3D_1$	464.647	470.048	474.953	$4d_{3/2}5d_{3/2}\ ^3P_0$	797.896	798.896	800.098
$4d_{5/2}5s_{1/2}\ ^3D_2$	452.403	456.956	462.274	$4d_{5/2}5d_{5/2}\ ^1S_0$	834.818	843.962	850.084
$4d_{3/2}5s_{1/2}\ ^1D_2$	471.295	473.496	478.377	$4d_{5/2}5d_{3/2}\ ^3S_1$	779.845	780.792	782.721
$4d_{5/2}5s_{1/2}\ ^3D_3$	450.649	453.468	458.936	$4d_{5/2}5d_{5/2}\ ^1P_1$	789.423	790.854	792.447
				$4d_{3/2}5d_{3/2}\ ^3P_1$	802.917	803.860	805.106
$4d_{3/2}5p_{3/2}\ ^3P_0$	607.570	607.906	610.152	$4d_{3/2}5d_{5/2}\ ^3D_1$	807.016	807.691	808.902
$4d_{5/2}5p_{3/2}\ ^3P_1$	589.358	594.592	598.038	$4d_{5/2}5d_{3/2}\ ^3D_2$	788.011	790.022	791.761
$4d_{3/2}5p_{1/2}\ ^1P_1$	601.998	604.877	608.162	$4d_{5/2}5d_{5/2}\ ^3P_2$	794.643	790.070	797.552
$4d_{3/2}5p_{3/2}\ ^3D_1$	616.912	618.269	621.353	$4d_{3/2}5d_{3/2}\ ^1D_2$	808.700	810.825	812.055
$4d_{5/2}5p_{1/2}\ ^3P_2$	569.187	575.438	580.213	$4d_{3/2}5d_{5/2}\ ^3F_2$	810.111	811.675	813.163
$4d_{5/2}5p_{3/2}\ ^3F_2$	590.465	591.154	597.942	$4d_{5/2}5d_{3/2}\ ^3D_3$	790.344	792.488	794.584
$4d_{3/2}5p_{1/2}\ ^1D_2$	600.537	602.541	606.623	$4d_{5/2}5d_{5/2}\ ^1F_3$	793.613	795.332	797.136
$4d_{3/2}5p_{3/2}\ ^3D_2$	618.074	621.147	624.510	$4d_{3/2}5d_{3/2}\ ^3G_3$	803.533	805.240	807.103
$4d_{5/2}5p_{1/2}\ ^3F_3$	575.957	578.986	584.299	$4d_{3/2}5d_{5/2}\ ^3F_3$	811.665	813.696	814.970
$4d_{5/2}5p_{3/2}\ ^3D_3$	602.436	605.410	609.128	$4d_{5/2}5d_{3/2}\ ^3G_4$	786.669	788.522	790.914
$4d_{3/2}5p_{3/2}\ ^1F_3$	613.858	616.157	619.300	$4d_{5/2}5d_{5/2}\ ^3F_4$	795.211	797.063	798.796
$4d_{5/2}5p_{3/2}\ ^3F_4$	594.369	596.854	600.514	$4d_{3/2}5d_{5/2}\ ^1G_4$	807.691	809.314	810.629
				$4d_{5/2}5d_{5/2}\ ^3G_5$	788.899	790.742	792.579
$4d_{5/2}4f_{5/2}\ ^3P_0$	652.795	662.461	664.012	$4d_{5/2}5f_{5/2}\ ^3P_0$	994.100	990.713	992.927
$4d_{5/2}4f_{5/2}\ ^3P_1$	655.104	665.447	666.724	$4d_{5/2}5f_{5/2}\ ^3P_1$	995.870	992.190	994.368
$4d_{5/2}4f_{7/2}\ ^3D_1$	687.124	696.312	697.257	$4d_{5/2}5f_{7/2}\ ^3D_1$	1007.095	1004.493	1006.755
$4d_{3/2}4f_{5/2}\ ^1P_1$	819.402	832.414	842.176	$4d_{3/2}5f_{5/2}\ ^1P_1$	1045.212	1036.871	1052.037
$4d_{5/2}4f_{5/2}\ ^3P_2$	662.600	670.544	672.121	$4d_{5/2}5f_{5/2}\ ^3P_2$	996.919	994.492	996.530
$4d_{5/2}4f_{7/2}\ ^1D_2$	683.618	689.957	690.948	$4d_{5/2}5f_{7/2}\ ^1D_2$	999.768	998.024	999.938
$4d_{3/2}4f_{5/2}\ ^3D_2$	691.734	699.289	700.035	$4d_{3/2}5f_{5/2}\ ^3D_2$	1013.613	1011.201	1012.718
$4d_{3/2}4f_{7/2}\ ^3F_2$	699.333	705.901	706.708	$4d_{3/2}5f_{7/2}\ ^3F_2$	1016.282	1014.147	1016.165
$4d_{5/2}4f_{5/2}\ ^3F_3$	685.066	690.460	691.584	$4d_{5/2}5f_{5/2}\ ^3F_3$	999.504	998.220	1000.228
$4d_{5/2}4f_{7/2}\ ^3D_3$	693.549	699.660	700.791	$4d_{5/2}5f_{7/2}\ ^1F_3$	1002.543	1001.354	1003.423
$4d_{3/2}4f_{5/2}\ ^3G_3$	708.293	712.655	713.611	$4d_{3/2}5f_{5/2}\ ^3D_3$	1017.290	1015.439	1017.514
$4d_{3/2}4f_{7/2}\ ^1F_3$	719.048	722.667	723.853	$4d_{3/2}5f_{7/2}\ ^3G_3$	1018.346	1017.377	1019.405
$4d_{5/2}4f_{5/2}\ ^3H_4$	683.342	690.311	691.244	$4d_{5/2}5f_{5/2}\ ^3F_4$	1000.564	998.989	1001.283
$4d_{5/2}4f_{7/2}\ ^3F_4$	686.232	692.368	693.903	$4d_{5/2}5f_{7/2}\ ^1G_4$	1001.151	999.783	1001.957
$4d_{3/2}4f_{5/2}\ ^1G_4$	698.488	704.102	704.989	$4d_{3/2}5f_{5/2}\ ^3H_4$	1014.290	1012.122	1014.231
$4d_{3/2}4f_{7/2}\ ^3G_4$	709.665	715.074	716.052	$4d_{3/2}5f_{7/2}\ ^3G_4$	1018.150	1017.029	1018.768
$4d_{5/2}4f_{5/2}\ ^3H_5$	675.642	682.823	683.650	$4d_{5/2}5f_{5/2}\ ^3H_5$	997.898	995.961	998.266
$4d_{5/2}4f_{7/2}\ ^1H_5$	691.234	697.763	698.281	$4d_{5/2}5f_{7/2}\ ^3G_5$	1001.660	1000.432	1002.584
$4d_{3/2}4f_{7/2}\ ^3G_5$	701.653	707.270	707.857	$4d_{3/2}5f_{7/2}\ ^1H_5$	1015.367	1013.617	1015.477
$4d_{5/2}4f_{7/2}\ ^3H_6$	672.161	679.529	680.870	$4d_{5/2}5f_{7/2}\ ^3H_6$	997.659	995.359	997.628

5. Magnetic-dipole, magnetic-quadrupole, and magnetic-octupole matrix elements

We calculate magnetic-dipole (M1) matrix elements for the transitions between the 11 even-parity $4d_j5s_{1/2}(1)$, $4d_j5d_{j'}(1)$, $4p_j5p_{j'}(1)$, $4p_j4f_{j'}(1)$, and $4p_j5f_{j'}(1)$ excited states and the ground state; the magnetic-quadrupole (M2) matrix elements between the 17 odd-parity $4d_j5p_{j'}(2)$, $4d_j4f_{j'}(2)$, $4d_j5f_{j'}(2)$, $4p_j5s_{1/2}(2)$, and $4p_j5d_{j'}(2)$ excited states and the ground state; and the magnetic-octupole (M3) matrix elements for the transitions between the 14 even-parity $4d_j5s_{1/2}(3)$, $4d_j5d_{j'}(3)$, $4p_j5p_{j'}(3)$, $4p_j4f_{j'}(3)$, and $4p_j5f_{j'}(3)$ excited states and the ground state for Pd-like ions with nuclear charges $Z = 47$–100.

We calculate first- and second-order Coulomb, second-order Breit–Coulomb corrections, and second-order derivative term to reduced M1, M2, and M3 matrix elements $Z^{(1)}$, $Z^{(2)}$, $B^{(2)}$, and $P^{(\mathrm{derv})}$, respectively, using the methods described in eqs. (2.13)–(2.18) of ref .28 and eqs. (A3)–(A5) of ref. 42, respectively. In this section, we illustrate the importance of the relativistic and frequency-dependent contributions to the first-order M1, M2, and M3 matrix elements. We also show the importance of taking into account the second-order RMBPT contributions to M1, M2, and M3 matrix elements, and we subsequently discuss the necessity of including the negative-energy contributions to sums over intermediate states. Ab initio relativistic calculations require careful treatment of negative-energy states (virtual electron–positron pairs). In second-order matrix elements, such contributions explicitly arise from those terms in the sum over states for which $\varepsilon_i < -mc^2$. The effect of the negative-energy states (NES) contributions to M1-amplitudes has been studied recently in ref. 33. The importance of the NES contributions varies with the transition. For example, the NES contributions to the second-order Breit–Coulomb matrix elements $B^{(2)}$ for the transition from $4d_{5/2}5d_{3/2}(1)$ state weakly

© 2008 NRC Canada

Table 8. Wavelengths (λ in Å) and weighted transition rates (gA in 10^9 s^{-1}) for odd-parity states with $J = 1$ in Pd-like ions with $Z = 54$–59. The RMBPT results are compared with experimental values "Expt." for wavelengths and transition rates "COWAN" presented in refs. 11 and 13.

	RMBPT	Expt.	RMBPT	COWAN	RMBPT	Expt.	RMBPT	COWAN
jj and LS.	λ	λ	gA	gA	λ	λ	gA	gA
	Pd-like Xe^{8+}				Pd-like Cs^{9+}			
$4d_{5/2}5p_{3/2}\ ^3P_1$	169.582		1.5		146.296	145.172	0.1	3.0
$4d_{3/2}5p_{1/2}\ ^1P_1$	166.081	165.323	235.4	264.8	143.402	142.890	323.1	343.3
$4d_{3/2}5p_{3/2}\ ^3D_1$	162.066	161.742	37.0	47.0	141.327	139.670	2.1	62.4
$4d_{5/2}4f_{5/2}\ ^3P_1$	152.647	150.275	0.7	0.7	139.913	139.534	58.5	1.4
$4d_{5/2}4f_{7/2}\ ^3D_1$	145.534	143.614	5.1	5.9	134.027	132.888	5.7	8.4
$4d_{3/2}4f_{5/2}\ ^1P_1$	121.998	120.133	3672.0	4766.0	110.918	109.589	5034.0	5992.0
$4d_{5/2}5f_{5/2}\ ^3P_1$	100.407		2.2		88.119		5.0	
$4d_{5/2}5f_{7/2}\ ^3D_1$	99.289	99.535	74.8	64.7	87.155	87.337	71.7	60.6
$4d_{3/2}5f_{5/2}\ ^1P_1$	95.670	96.449	1235.4	1516.0	84.529	85.052	805.5	916,8
	Pd-like Ba^{10+}				Pd-like La^{11+}			
$4d_{5/2}5p_{3/2}\ ^3P_1$	132.007		0.8		124.055		0.9	
$4d_{3/2}5p_{1/2}\ ^1P_1$	127.772	126.908	0.8	9.9	116.944	116.473	5.7	8.8
$4d_{3/2}5p_{3/2}\ ^3D_1$	125.140	125.042	207.2	441.7	112.806	112.107	4.8	26.9
$4d_{5/2}4f_{5/2}\ ^3P_1$	124.983	124.001	244.7	26.0	110.765	110.514	583.2	581.9
$4d_{5/2}4f_{7/2}\ ^3D_1$	122.250	122.103	76.6	87.2	107.975	107.959	108.1	116.2
$4d_{3/2}4f_{5/2}\ ^1P_1$	102.309	101.391	6078.0	7471.0	95.396	94.764	6948.0	9476.0
$4d_{5/2}5f_{5/2}\ ^3P_1$	78.194		44.2		70.033		192.4	
$4d_{5/2}5f_{7/2}\ ^3D_1$	77.365		9.4		69.322		23.4	
$4d_{3/2}5f_{5/2}\ ^1P_1$	75.436		381.6		67.838		73.8	
	Pd-like Ce^{12+}				Pd-like Pr^{13+}			
$4d_{5/2}5p_{3/2}\ ^3P_1$	117.174		0.9		111.144	109.900	1.1	1.3
$4d_{3/2}5p_{1/2}\ ^1P_1$	110.260	109.945	7.7	13.3	104.436	104.225	9.7	13.
$4d_{3/2}5p_{3/2}\ ^3D_1$	100.516	99.936	12.9	61.8	90.256	89.773	23.7	97.
$4d_{5/2}4f_{5/2}\ ^3P_1$	98.718	98.535	761.7	787.6	88.662	88.513	1055.7	1056.
$4d_{5/2}4f_{7/2}\ ^3D_1$	96.180	96.091	156.2	141.2	86.354	86.274	271.6	251.
$4d_{3/2}4f_{5/2}\ ^1P_1$	89.680	89.237	7518.0	9434.0	84.779	84.500	7890.0	9532.
$4d_{5/2}5f_{5/2}\ ^3P_1$	63.216		34.9		57.449		435.3	
$4d_{5/2}5f_{7/2}\ ^3D_1$	62.607		153.5		56.925		268.3	
$4d_{3/2}5f_{5/2}\ ^1P_1$	61.397		8.1		55.885		92.0	

increases with Z, however, the relative NES contribution for this transition decreases with Z (2% and 0.6% for $Z = 50$ and $Z = 90$, respectively). It should be noted that the NES contribution for this transition is of the same order as the positive-energy state contribution to the second-order Breit–Coulomb matrix elements causing severe cancellation and drastically reducing the $B^{(2)}$ values in this case.

5.1. Z-dependences of M1, M2, and M3 matrix elements in Pd-like ions

The differences between first-order M1 uncoupled matrix elements, calculated in nonrelativistic, relativistic frequency-independent, and relativistic frequency-dependent approximations are illustrated in the left top panel of Fig. 7 for the $0 - 4d_{5/2}5d_{5/2}(1)$ matrix element. The corresponding matrix elements are labeled $Z^{(1)}_{\rm RF}$, $Z^{(1)}_{\rm R}$, and $Z^{(1)}_{\rm NR}$. Formulas for relativistic frequency-dependent and nonrelativistic first-order M1 matrix elements are given by eqs. (A8)–(A12) of ref. 31. We also plot the second-order Coulomb contributions, $Z^{(2)}_{\rm CL}$, and the second-order Breit–Coulomb contributions, $Z^{(2)}_{\rm BR}$, in the same figure. As we observe from the left panel of Fig. 7, the values of $Z^{(1)}_{\rm NR}$ are twice as small as the values of $Z^{(1)}_{\rm R}$ and $Z^{(1)}_{\rm RF}$. Therefore, relativistic effects are very large for M1 transitions. The frequency-dependent relativistic matrix elements $Z^{(1)}_{\rm RF}$ differ from the relativistic frequency-independent matrix elements $Z^{(1)}_{\rm R}$ by 50–90%. The differences between other first-order matrix elements calculated with and without frequency dependence are also on the order of a few percent. Uncoupled second-order M1 matrix elements, $Z^{(2)}_{\rm CL}$, are comparable in size to the first-order matrix elements $Z^{(1)}_{\rm RF}$ for small Z, but the relative size of the second-order contribution decreases for high Z. This is expected since second-order Coulomb matrix elements $Z^{(2)}_{\rm CL}$ are proportional to Z for high Z while first-order matrix elements $Z^{(1)}_{\rm RF}$ grow as Z^2. The second-order Breit–Coulomb matrix elements $Z^{(2)}_{\rm BR}$ are proportional to Z^3 and become larger than $Z^{(2)}_{\rm CL}$ for high Z.

The differences between the first-order M2 uncoupled matrix elements for the $0 - 4d_{5/2}5p_{1/2}(2)$ matrix element, calculated in relativistic frequency-independent $Z^{(1)}_{\rm R}$, and relativis-

© 2008 NRC Canada

Fig. 9. E1, E2, and M3 transition rates (gA_r) for transitions between odd- and even-parity states and ground state in Pd-like ions as function of Z.

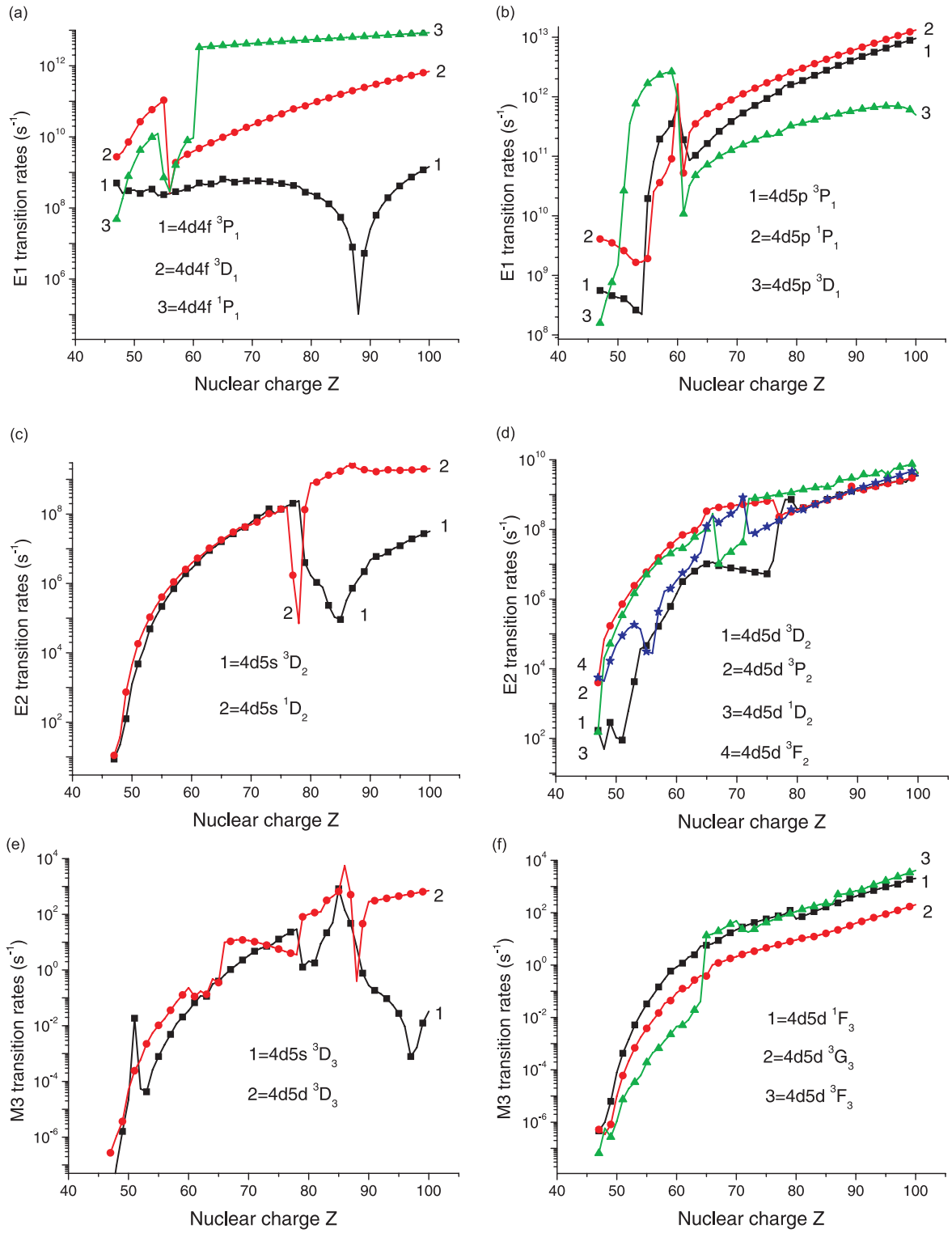

tic frequency-dependent $Z_{\mathrm{RF}}^{(1)}$ approximations are very small (about 1%), and we include only $Z_{\mathrm{RF}}^{(1)}$ in the right top panel of Fig. 7. Formulas for relativistic frequency-dependent and frequency-independent first-order M2 matrix elements are given by eqs. (A3)–(A5) of ref. 42. We also plot the second-order Coulomb contributions, $Z_{\mathrm{CL}}^{(2)}$, and the second-order Breit–Coulomb contributions, $Z_{\mathrm{BR}}^{(2)}$, in the same figure. We observe the sharp features around $Z = 78$ in the curves illustrating

© 2008 NRC Canada

Fig. 10. M1, M2, and E3 transition rates (gA_r) for transitions between odd- and even-parity states and the ground state in Pd-like ions as function of Z.

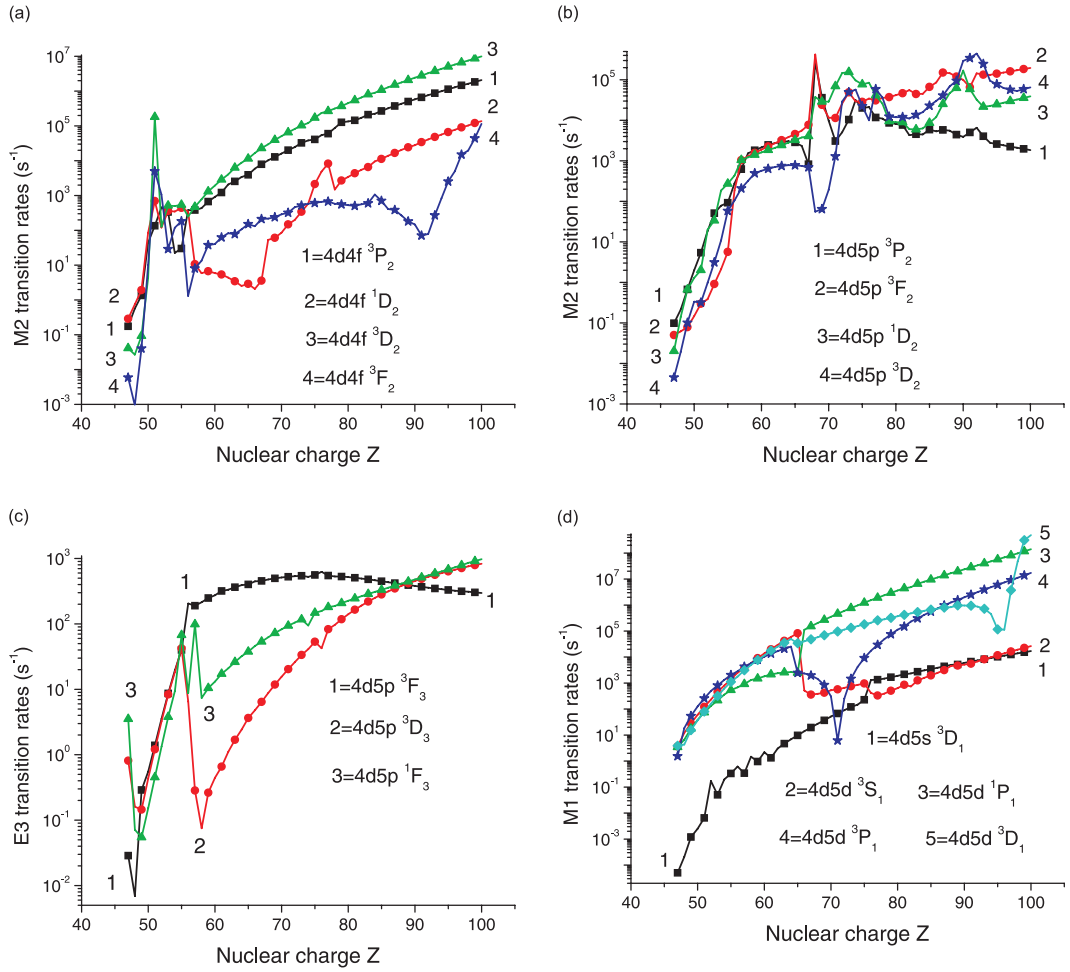

the $Z^{(2)}_{\rm CL}$ and $Z^{(2)}_{\rm BR}$ trends. Those features result from very small values of the denominators in the second-order contributions $Z^{(2)}_{\rm CL}$ and $Z^{(2)}_{\rm BR}$ [8].

Similar features are observed in the second-order Coulomb contributions, $Z^{(2)}_{\rm CL}$, and the second-order Breit–Coulomb contributions, $Z^{(2)}_{\rm BR}$ for the $0-4d_{5/2}5s_{1/2}(3)$ magnetic-octupole matrix element in the bottom panel of Fig. 7.

In Fig. 8, we illustrate the Z-dependence of the line strengths of M1 transition from the $4d5s\ ^3D_1$ excited state to the ground state. It should be noted that the line strength is defined as a square of a coupled matrix element. In Fig. 8, we plot the values of the first-order line strengths $S^{(1)}_{\rm NR}$, $S^{(1)}_{\rm R}$, and $S^{(1)}_{\rm RF}$ calculated in the same approximations as the M1 uncoupled matrix elements: nonrelativistic, relativistic frequency-independent, and relativistic frequency-dependent approximations, respectively. The total line strengths $S^{(1+2)}$, which include second-order corrections, are also plotted. It should be noted that the value of the nonrelativistic matrix element, $Z^{(1)}_{\rm NR}(0-4d_{5/2}5s_{1/2}(1))$, is equal to zero. Small mixing inside of the even-parity complex with $J=1$ between $4d_{5/2}5s_{1/2}$, $4d_j5d_{j'}$, and $4p_j5p_{j'}$ states gives a nonzero value of the first-order coupled matrix element and, consequently, the line strengths $S^{(1)}_{\rm NR}$ even for $Z=47$. However, the value of $S^{(1)}_{\rm NR}$ is smaller than the value of $S^{(1)}_{\rm R}$ by one order of magnitude at $Z=47$. The difference between the values of $S^{(1)}_{\rm R}$ and $S^{(1)}_{\rm RF}$ is 36% for $Z=47$. The second-order contribution gives an additional contribution for the value of the line strengths, and the ratio of $S^{(1+2)}_{\rm RF}$ and $S^{(1)}_{\rm RF}$ is about 15 for $Z=47$. The ratios between $S^{(1)}_{\rm NR}$, $S^{(1)}_{\rm R}$, $S^{(1)}_{\rm RF}$, and $S^{(1+2)}_{\rm RF}$ change with Z owing to increasing relativistic effects. The abrupt change in the values of the $S^{(1)}_{\rm NR}$ at $Z=76$ happens because of very strong mixing between the $4d_{5/2}5s_{1/2}(1)$ and $4p_{3/2}4f_{5/2}(1)$ states (see Fig. 3). It should be noted that the $Z^{(1)}_{\rm NR}(0-4p_{3/2}4f_{5/2}(1))$ value is zero and, as a result, we observe a sharp (three order of magnitude) decrease in the value of $S^{(1)}_{\rm NR}$ at $Z\geq 76$.

5.2. E1, E2, E3, M1, M2, and M3 transition rates

The E1, E2, E3, M1, M2, and M3 transition probabilities A_r (s^{-1}) for the transitions between the ground state and $4lj4fj'(J)$, $4lj5l'j'(J)$ states are obtained in terms of line strengths S (a.u.) and wavelength λ(Å) as

© 2008 NRC Canada

$$A(E1) = \frac{2.02613 \times 10^{18}}{(2J+1)\lambda^3} S(E1), \qquad A(M1) = \frac{2.69735 \times 10^{13}}{(2J+1)\lambda^3} S(M1)$$
$$A(E2) = \frac{1.11995 \times 10^{18}}{(2J+1)\lambda^5} S(E2), \qquad A(M2) = \frac{1.49097 \times 10^{13}}{(2J+1)\lambda^5} S(M2)$$
$$A(E3) = \frac{3.14441 \times 10^{17}}{(2J+1)\lambda^7} S(E3), \qquad A(M3) = \frac{4.18610 \times 10^{12}}{(2J+1)\lambda^7} S(M3) \tag{3}$$

In the tables and figures below, we present our RMBPT calculations for E1, E2, E3, M1, M2, and M3 transition rates and wavelengths.

6. Comparison of results with other theory and experiment

We calculate energies of the 56 even-parity $4d_j5s_{1/2}(J)$, $4d_j5d_{j'}(J)$, $4p_j5p_{j'}(J)$, $4p_j4f_{j'}(J)$, and $4p_j5f_{j'}(J)$ excited states and 68 odd-parity $4d_j5p_{j'}(J)$, $4d_j4f_{j'}(J)$, $4d_j5f_{j'}(J)$, $4p_j5s_{1/2}(J)$, and $4p_j5d_{j'}(J)$ excited states for Pd-like ions with nuclear charges $Z = 47$–100. Reduced matrix elements, oscillator strengths, and transition rates are determined for E1-, E2-, E3-, M1-, M2-, and M3-allowed and forbidden transitions into the ground state for each ion. Comparisons are also given with other theoretical results and with experimental data. Our results are presented in two parts: wavelengths and transition probabilities.

6.1. Transition energies

In Table 7, we compare our RMBPT results for the excitation energies of the odd-parity states in Pd-like xenon with theoretical results obtained by COWAN code [43] and experimental data presented by Churilov et al. [11]. The experimental results were confirmed by semi-empirical calculations in the frames of the Cowan code and Generalized Least-Square techniques [11]. Our RMBPT results differ from the results presented in ref. 11 by about 0.1–0.5% for most of the levels, except the $4dj4fj'$ J levels when the disagreement is about 0.5–1.5%. We can see from Table 7 that the RMBPT values are smaller than the experimental values, however, the COWAN values are larger than experimental values in many cases. Correlation effects in the COWAN code are included by taking into account additional configurations ($4p^64d^{10}+4p^64d^95s+4p^64d^95d+4p^64d^96s+4p^64d^96d+4p^54d^104f+4p^54d^105p+4p^54d^105f$ and $4p^64d^95p + 4p^64d^94f + 4p^64d^96p + 4p^64d^95f + 4p^54d^105s + 4p^54d^105d$) and scaled Hartree–Fock (HF) integrals. Only one scaling factor, 0.85, is used in the results given in the column headed COWAN in Table 7. The labelling of the levels in ref. 11 was based on the COWAN code. It should be noted that the RMBPT code used jj-coupling; however, the COWAN code used LS-coupling for uncoupled matrix elements. To compare the results obtained after diagonalization of the energy matrixes in Table 7, we use both the jj and LS designations. The LSJ labels in the RMBPT code are chosen by searching for small values of multiplet splitting for low-Z ions. We found that resulting LS designations in RMBPT and COWAN codes differ for some states. In the COWAN code, a label for every level was chosen as a maximum value among eigenvectors. As a result, two levels can have the same label. It is known that the crossing of energy levels inside one complex with the same J is forbidden by the Wigner and Neumann theorem (see, for example, ref. 40). As a result, we can use only the numbering of the levels by ordering of energies. We already mentioned that either LS or jj designations are used to label the resulting eigenvectors and eigenvalues rather than simply enumerating levels with an index N. We choose the LS designations here since the jj designations are used for uncoupled matrix elements.

6.2. E1, E2, E3, M1, M2, and M3 transition probabilities

We present the resulting transition probabilities (A_r) in Figs. 9 and 10. Transition rates for the six E1 transitions from the $4d5p\ ^3P_1$, $^1P_1$, $^3D_1$, and $4d4f\ ^3P_1$, $^3D_1$, $^1P_1$ levels to the ground state are plotted in the top panel of Fig. 9. The deep minimum in the curves labeled $4d4f\ ^3P_1$ ($Z = 88$), and $4d5p\ ^3D_1$ ($Z = 56$) are due to mixing of $[4d_{5/2}4f_{5/2}(1) + 4d_{5/2}4f_{7/2}(1)]$ and $[4d_{3/2}5p_{1/2}\ (1) + 4d_{5/2}5p_{3/2}\ (1)]$ states, respectively. It should be noted that the mixing of those states is not very large (about 15–20%) in the first case, but the ratios of corresponding dipole-matrix elements are equal to 4–5, and the sign of these ratios is different from the sign of the corresponding ratio of mixing coefficients. This leads to cancellation since the coupled matrix elements are products of matrix elements and mixing coefficients. As a result, deep minima occur in the curve illustrated the transition from the $4d4f\ ^3P_1$ state at $Z = 88$ (see also ref. 8).

Transition rates for the six E2 transitions from $4d5s\ ^3D_2$, $^1D_2$ and $4d5d\ ^3D_2$, $^3P_2$, $^1D_2$, $^3F_2$ levels to the ground state are plotted in the central panel of Fig. 9. The curves describing $4d5s\ ^3D_2$, $^1D_2$ transition rates smoothly increase with Z up to $Z = 75$ without any sharp features. The difference in values of A_r for $4d5s\ ^3D_2$ and $4d5s\ ^1D_2$ lines is about 20–50%. The deep minimum in the curve labeled $4d5s\ ^3D_2$ ($Z = 79$–82) is due to mixing of the $[4d_{3/2}5s_{1/2}\ (2) + 4p_{3/2}4f_{5/2}\ (2)]$ states (see the Z-dependence of mixing coefficients for the $4d5d\ ^3D_2$ states on the right panel of Fig. 3). The deep, sharp minimum in the curve labeled $4d5s\ ^1D_2$ ($Z = 77$–78) happens because of strong mixing of the $[4d_{5/2}5s_{1/2}\ (2) + 4p_{3/2}4f_{5/2}\ (2)]$, $[4d_{5/2}5s_{1/2}\ (2) + 4d_{3/2}5s_{1/2}\ (2)]$, and $[4d_{5/2}5s_{1/2}\ (2) + 4p_{3/2}4f_{7/2}\ (2)]$ states at $Z = 77$–78, $Z = 79$, and $Z \geq 80$, respectively. There are no large differences in the values of transition rates illustrated on the right central panel of Fig. 9 due to strong mixing between the states $4d_j5d_{j'}\ (2)$ with $j = 3/2$, 5/2, and $j' = 3/2$, 5/2.

Transition rates for the five M3 transitions from the $4d5s\ ^3D_3$, and $4d5d\ ^3G_3$, $^3D_3$, $^3F_3$, $^1F_3$ levels to the ground state are plot-

© 2008 NRC Canada

Table 9. Wavelengths (λ in Å) and multipole (E1, E2, E3, M1, M2, and M3) transition rates (A_r in s^{-1}) for Pd-like Yb^{24+}, Hg^{34+}, Th^{44+}, and U^{46+}. Numbers in brackets represent powers of 10.

	Yb^{24+}		Hg^{34+}		Th^{44+}		U^{46+}	
Level	λ	A_r	λ	A_r	λ	A_r	λ	A_r
Magnetic-dipole transitions, M1								
$4d_{3/2}5s_{1/2}\ ^3D_1$	42.931	5.08[01]	27.163	1.92[03]	21.487	1.92[03]	20.571	7.51[03]
$4d_{5/2}5d_{3/2}\ ^3S_1$	35.880	5.34[02]	24.769	6.37[02]	16.455	6.37[02]	15.345	6.82[03]
$4d_{5/2}5d_{5/2}\ ^1P_1$	31.374	3.53[05]	18.825	3.61[06]	12.673	3.61[06]	11.821	3.36[07]
$4d_{3/2}5d_{3/2}\ ^3P_1$	30.955	3.05[02]	18.516	1.13[05]	12.406	1.13[05]	11.558	3.14[06]
$4d_{3/2}5d_{5/2}\ ^3D_1$	30.285	8.13[04]	18.082	3.67[05]	12.052	3.67[05]	11.217	8.65[05]
Electric-quadrupole transitions, E2								
$4d_{5/2}5s_{1/2}\ ^3D_2$	44.566	5.68[07]	27.162	1.66[06]	21.433	1.66[06]	20.513	6.24[08]
$4d_{3/2}5s_{1/2}\ ^1D_2$	42.691	4.91[07]	26.157	7.65[08]	20.597	7.65[08]	19.694	3.66[07]
$4d_{5/2}5d_{3/2}\ ^3D_2$	35.898	7.30[06]	26.055	3.77[08]	17.560	3.77[08]	16.434	1.60[09]
$4d_{5/2}5d_{5/2}\ ^3P_2$	34.486	4.73[08]	24.738	3.16[08]	16.434	3.16[08]	15.328	1.38[09]
$4d_{3/2}5d_{3/2}\ ^1D_2$	31.177	3.35[07]	21.004	1.27[09]	14.965	1.27[09]	13.987	3.45[09]
$4d_{3/2}5d_{5/2}\ ^3F_2$	30.814	3.69[08]	18.733	3.12[08]	12.624	3.12[08]	11.776	1.91[09]
Magnetic-octupole transitions, M3								
$4d_{5/2}5s_{1/2}\ ^3D_3$	44.656	3.24[00]	26.822	2.05[00]	21.226	2.05[00]	20.324	1.40[01]
$4d_{5/2}5d_{3/2}\ ^3D_3$	35.456	1.13[01]	26.497	1.01[02]	20.781	1.01[02]	19.855	3.41[02]
$4d_{5/2}5d_{5/2}\ ^1F_3$	35.204	2.22[01]	26.097	5.77[01]	17.587	5.77[01]	16.457	5.98[02]
$4d_{3/2}5d_{3/2}\ ^3G_3$	31.119	2.06[00]	21.400	8.85[00]	15.125	8.85[00]	14.129	5.35[01]
$4d_{3/2}5d_{5/2}\ ^3F_3$	30.824	4.84[01]	21.234	1.07[02]	14.900	1.07[02]	13.901	9.38[02]
Electric-dipole transitions, E1								
$4d_{5/2}5p_{3/2}\ ^3P_1$	72.695	5.72[08]	55.955	2.53[08]	45.584	2.53[08]	43.957	1.17[08]
$4d_{3/2}5p_{1/2}\ ^1P_1$	67.431	2.17[10]	50.970	8.62[10]	40.473	8.62[10]	38.800	3.35[11]
$4d_{3/2}5p_{3/2}\ ^3D_1$	55.507	3.86[12]	42.355	5.00[12]	33.663	5.00[12]	32.231	6.69[12]
$4d_{5/2}4f_{5/2}\ ^3P_1$	37.813	4.43[11]	22.303	1.66[12]	15.005	1.66[12]	14.015	5.12[12]
$4d_{5/2}4f_{7/2}\ ^3D_1$	36.830	9.86[11]	21.503	2.74[12]	14.204	2.74[12]	13.208	7.32[12]
$4d_{3/2}4f_{5/2}\ ^1P_1$	35.583	1.39[11]	20.634	3.36[11]	13.477	3.36[11]	12.502	6.42[11]
$4d_{5/2}5f_{5/2}\ ^3P_1$	27.577	1.16[12]	17.545	3.45[12]	12.315	3.45[12]	11.579	9.72[12]
$4d_{5/2}5f_{7/2}\ ^3D_1$	26.259	1.19[11]	16.138	1.93[11]	11.008	1.93[11]	10.292	1.19[10]
$4d_{3/2}5f_{5/2}\ ^1P_1$	26.083	3.13[12]	16.028	1.51[13]	10.921	1.51[13]	10.204	5.04[13]
Magnetic-quadrupole transitions, M2								
$4d_{5/2}5p_{1/2}\ ^3P_2$	71.062	9.74[03]	54.533	8.14[03]	44.457	8.14[03]	42.886	6.55[03]
$4d_{5/2}5p_{3/2}\ ^3F_2$	69.387	1.16[04]	53.150	4.19[04]	42.666	4.19[04]	40.979	1.44[05]
$4d_{3/2}5p_{1/2}\ ^1D_2$	66.007	2.90[04]	48.897	8.91[03]	37.847	8.91[03]	36.066	2.23[00]
$4d_{3/2}5p_{3/2}\ ^3D_2$	65.271	1.92[02]	48.115	1.20[04]	36.774	1.20[04]	34.930	4.46[05]
$4d_{5/2}4f_{5/2}\ ^3P_2$	39.369	1.58[04]	23.488	1.33[05]	16.003	1.33[05]	14.993	7.59[05]
$4d_{5/2}4f_{7/2}\ ^1D_2$	37.834	8.44[01]	22.384	3.41[03]	15.047	3.41[03]	14.054	4.06[04]
$4d_{3/2}4f_{5/2}\ ^3D_2$	36.864	5.02[04]	21.519	4.49[05]	14.215	4.49[05]	13.218	3.26[06]
$4d_{3/2}4f_{7/2}\ ^3F_2$	35.538	2.84[02]	20.570	5.23[02]	13.446	5.23[02]	12.475	7.80[01]
$4d_{5/2}5f_{5/2}\ ^3P_2$	27.628	1.18[05]	17.574	8.48[05]	12.332	8.48[05]	11.595	4.46[06]
$4d_{5/2}5f_{7/2}\ ^1D_2$	26.192	2.99[05]	16.099	1.46[06]	10.984	1.46[06]	10.269	2.60[06]
$4d_{3/2}5f_{5/2}\ ^3D_2$	26.121	3.52[05]	16.053	5.93[06]	10.940	5.93[06]	10.222	5.20[07]
$4d_{3/2}5f_{7/2}\ ^3F_2$	25.527	2.50[03]	15.590	1.52[04]	10.533	1.52[04]	9.827	2.39[06]
Electric-octupole transitions, E3								
$4d_{5/2}5p_{1/2}\ ^3F_3$	69.612	5.54[02]	53.743	5.48[02]	43.904	5.48[02]	42.360	3.73[02]
$4d_{5/2}5p_{3/2}\ ^3D_3$	67.630	1.67[01]	51.636	1.53[02]	41.461	1.53[02]	39.831	5.77[02]
$4d_{3/2}5p_{3/2}\ ^1F_3$	64.503	8.63[01]	47.818	2.38[02]	37.089	2.38[02]	35.359	5.79[02]
$4d_{5/2}4f_{5/2}\ ^3F_3$	63.754	3.45[00]	47.057	5.50[01]	35.987	5.50[01]	34.189	3.22[02]
$4d_{5/2}4f_{7/2}\ ^3D_3$	39.223	1.24[04]	23.427	1.06[05]	15.971	1.06[05]	14.964	6.41[05]
$4d_{3/2}4f_{5/2}\ ^3G_3$	36.742	1.39[04]	21.459	1.37[05]	14.181	1.37[05]	13.188	1.06[06]
$4d_{3/2}4f_{7/2}\ ^1F_3$	35.619	1.91[04]	20.627	2.22[05]	13.473	2.22[05]	12.498	1.91[06]
$4d_{5/2}5f_{5/2}\ ^3F_3$	26.135	1.28[05]	16.072	9.42[05]	10.970	9.42[05]	10.257	5.71[06]
$4d_{5/2}5f_{7/2}\ ^1F_3$	26.064	2.12[05]	16.021	2.00[06]	10.917	2.00[06]	10.201	1.36[07]
$4d_{3/2}5f_{5/2}\ ^3D_3$	25.469	2.06[05]	15.544	1.58[06]	10.512	1.58[06]	9.808	9.86[06]
$4d_{3/2}5f_{7/2}\ ^3G_3$	25.443	5.71[01]	15.525	2.45[05]	10.477	2.45[05]	9.770	3.45[06]

© 2008 NRC Canada

ted in the bottom panel of Fig. 9. The sharp features in the curves shown in these figures are explained in many cases by strong mixing of states inside of the even-parity [$4d_{5/2}5s_{1/2}$ (3) + $4p_{3/2}4f_{5/2}$ (3)] and [$4d_{5/2}5d_j$ (3) + $4p_{3/2}4f_j$ (3)] complexes. For example, the $4d_{5/2}5d_{3/2}$ (3) state gives the dominant contribution to the transition rate A_r for transitions from the $4d5d\,^3D_3$ level up to $Z = 65$, but two other states, $4p_{3/2}4f_{5/2}$ (3) and $4p_{3/2}4f_{7/2}$ (3), give the dominant contributions for $Z > 65$. The $4d_{5/2}5s_{1/2}$ (3) state about 90% to A_r of the $4d5d\,^3D_3$ transitions for $Z = 79$ contributes. Such a complicated change of the dominant contributions is a main source of the sharp features in the transition rates for the M3 lines presented on the bottom panel of Fig. 9.

Transition rates for the eight M2 lines from $4d4f\,^3P_2$, $^1D_2$, $^3D_2$, $^3F_2$ and $4d5p\,^3P_2$, $^3F_2$, $^1D_2$, $^3D_2$ and $4d4f\,^3P_2$, $^1D_2$, $^3D_2$, $^3F_2$ levels to the ground state are plotted in top panel of Fig. 10. We can see the similarity of these figures with the figures describing E1 transition rates shown on the top panel of Fig. 9. For example, the dominant contribution for the transition rates from the $4d5p\,^3P_2$ level arises from the $4d_{5/2}5p_{1/2}$ (2) state for $Z = 47$–56. For high-Z ions, the contribution of this state completely disappears, but the contribution of the four $4d_j4f_{j'}$ (2) states ($j = 5/2$, 7/2, and $j' = 5/2$, 7/2) become significant for $Z = 57$–100. The contributions of each of the $4d_j4f_{j'}$ (2) states change from 50% to 5% with Z. The dominant contribution for the transition rates from the $4d4f\,^3P_2$ level comes from the $4d_{5/2}5p_{1/2}$ (2) state for $Z \geq 58$. For small-Z ions, the contribution of this state completely disappears, but the contributions of the two $4d_{5/2}4f_{5/2}$ (2) and $4d_{5/2}4f_{7/2}$ (2) states dominate for $Z = 50$–54; the contributions of the $4d_{5/2}5p_{1/2}$ (2), $4d_{3/2}5p_{3/2}$ (2), $4d_{5/2}5p_{3/2}$ (2), and $4d_{3/2}4f_{5/2}$ (2) dominate for $Z = 47$–49, 55, 56, and 57, respectively. Such a complicated change of dominant contributions leads to the very sharp features for the small-Z ions that we observe for all curves shown in the left top panel of of Fig. 10.

Transition rates for the three E3 transitions from $4d5p\,^3F_3$, $^3D_3$, $^1F_3$ levels to the ground state are plotted in the left bottom panel of Fig. 10. The dominant contribution for the transition rates for these three E3 lines changes at $Z = 55$. For low-Z ions, the $4d_j5d_{j'}$ (3) states determine the values of A_r, but for high-Z ions the contribution of the $4d_j4f_{j'}$ (3) states dominates for the values of A_r for the three E3 $4d5p$ lines. As a result of this change in the dominant configurations around $Z = 55$, we find the sharp features in curves in this region of Z.

Transition rates for the five M1 lines from $4d5s\,^3D_1$ and $4d5d\,^3S_1$, $^1P_1$, $^3P_1$, $^3D_1$ levels to the ground state are plotted in the right bottom panel of Fig. 10. The deep minima for $Z = 71$ in the curve with the $4d5d\,^3P_1$ label is explained by strong mixing between $4d_{5/2}5d_{5/2}$ (1) $4d_{3/2}5d_{3/2}$ (1), and $4d_{3/2}5d_{5/2}$ (1) states. The largest mixing coefficient for the $4d5d\,^3P_1$ levels changes at $Z = 65$, it is the $C^N[4d_{3/2}5d_{3/2}(1)]$ for the small-Z ions and $C^N[4d_{5/2}5d_{5/2}(1)]$ for the high-Z ions. The $C^N[4d_{3/2}5d_{5/2}(1)]$ mixing coefficient slowly decreases from 0.78 for $Z = 48$ to 0.08 for $Z = 71$. However, the $Z^{(1+2)}(0 - 4d_{3/2}5d_{5/2}(1))$ matrix element is larger than the $Z^{(1+2)}(0 - 4d_{3/2}5d_{3/2}(1))$ and $Z^{(1+2)}(0 - 4d_{5/2}5d_{5/2}(1))$ matrix elements by factors five and three, respectively. As a result, a competition between three contributions (the product of the mixing coefficients and magnetic matrix elements) leads to the deep minimum at $Z = 71$ in the curve describing transition rates for the $4d5d\,^3P_1$ line presented in the right bottom panel of Fig. 10.

In Table 8, wavelengths and electric-dipole weighted transition rates are presented for the nine transitions from the $4d5p$, $4d4f$, and $4d5f$ states into the ground state in Pd-like Xe^{8+}, Cs^{9+}, Ba^{10+}, La^{11+}, Ce^{12+}, and Pr^{13+}. The RMBPT results are compared with the experimental measurements of Churilov et al. in refs. 11 and 13. We can see from Table 8 that our wavelength results are in good agreement (0.1–0.5%) with experimental measurements, except in the case of the $4d4f$ states in Pd-like Xe^{8+}. The case of Pd-like Xe^{8+} was discussed in detail previously, and the energies of the 74 states of Pd-like xenon were presented in Table 7. Our weighted transition rates gA_r for the transitions from the $4d5p$, $4d4f$, and $4d5f$ states into the ground state are compared with gA_r given in refs. 11 and 13. Results for gA_r agree in most cases, but those gA_r do not agree with the relative intensities given in refs. 11 and 13. We need additional calculations to build synthetic spectra to make the comparison with the relative intensities.

In Table 9, wavelengths and multipole (E1, E2, E3, M1, M2, and M3) transition rates are presented for Pd-like Yb^{24+}, Hg^{34+}, Th^{44+}, and U^{46+}. We include the 48 multipole transitions from $4d5s$, $4d5p$, $4d5d$, $4d4f$, and $4d5f$ states. Both, jj and LS labelling of states are given in Table 9. We compare our RMBPT results for energies with results calculated using the multiconfiguration Dirac–Fock (MCDF) approach, presented in ref. 17. The difference between the RMBPT and MCDF results is about 0.1–0.5%. The largest disagreement (1%) is found for the $4d_{5/2}5p_{3/2}\,^3P_1$ level. We find disagreement in identification of even-parity states for ions with $Z = 80$, 90, and 92; $4d5d$ instead of $4d5s$. RMBPT and MCDF results for transition rates agree to 10–20% for few multipole transitions that were given in ref. 17, except for one M3 transition.

7. Conclusion

In this paper, we have presented a systematic second-order relativistic many-body perturbation theory study of excitation energies, reduced matrix elements, line strengths, and transition rates for $4d^{-1}4f$, $4d^{-1}5s$, $4d^{-1}5p$, $4d^{-1}5d$, $4d^{-1}5f$, $4p^{-1}4f$, $4p^{-1}5s$, $4p^{-1}5p$, $4p^{-1}5d$, and $4p^{-1}5f$ electric- and magnetic-dipole, electric- and magnetic-quadrupole, and electric- and magnetic-octupole transitions in Pd-like ions with nuclear charges $Z = 47$–100. Our calculations of the retarded E1, E2, E3, M1, M2, and M3 matrix elements include correlation corrections from both Coulomb and Breit interactions. Contributions from virtual electron–positron pairs were also included in the second-order matrix elements. Both length and velocity forms of the E1, E2, and E2 matrix elements were evaluated and small differences, caused by the nonlocality of the starting DF potential, were found between the two forms. Second-order RMBPT transition energies were used to evaluate oscillator strengths and transition rates. Good agreement of our RMBPT data with other theoretical results is found. Results from the present calculations provide benchmark values for future theoretical and experimental studies of the palladium isoelectronic sequence.

References

1. G. O'Sullivan, A. Cummings, P. Dunne, K. Fahy, P. Hayden, L. McKinney, N. Murphy, E. Sokell, and J. White. AIP Conf.

© 2008 NRC Canada

Proc. **771**, 108 (2005).
2. F. Gilleron, M. Poirier, T. Blenski, M. Schmidt, and T. Ceccotti. J. Appl. Phys. **94**, 2086 (2003).
3. K. Fahy, P. Dunne, L. McKinney, G. O'Sullivan, E. Sokell, J. White, A. Aguilar, J.M. Pomeroy, J.N. Tan, and B. Blagojević. J. Phys. D, **37**, 3232 (2004).
4. J.R. Crespo Lopez-Urrutia. P. Beiersdorfer, K. Widmann, and V. Decaux. Phys. Scr. **T80**, 448 (1999).
5. C. Biedermann, R. Radtke, G. Fußmann, J.-L. Schwob, and P. Mandelbaum. Nucl. Instrum. Meth. Phys. Res. B, **235**, 126 (2005).
6. N. Böwering, M. Martins, W.N. Partlo, and I.V. Fomenkov. J. App. Phys. **95**, 16 (2004).
7. H. Merabet, S. Kondagari, R. Bruch, S. Fülling, S. Hahto, K.-L. Leung, J. Reijonen, A.L. Godunov, and V.A. Schipakov. Nucl. Instrum. Meth. Phys. Res. B, **241**, 23 (2005).
8. U.I. Safronova, T.E. Cowan, and W.R. Johnson. Can. J. Phys. **83**, 813 (2005).
9. S.S. Churilov, Y.N. Joshi, and A.N. Ryabtsev. J. Phys. B, **27**, 5485 (1994).
10. S.S. Churilov, V.A. Azarov, A.N. Ryabtsev, W.-Ü.L. Tchang-Brillet, and J.-F. Wyart. Phys. Scr. **61**, 420 (2000).
11. S.S. Churilov, A.N. Ryabtsev, W.-Ü.L. Tchang-Brillet, and J.-F. Wyart. Phys. Scr. **66**, 293 (2002).
12. S.S. Churilov, A.N. Ryabtsev, W.-Ü.L. Tchang-Brillet, and J.-F. Wyart. Phys. Scr. **T100**, 98 (2002).
13. S.S. Churilov, A.N. Ryabtsev, J.-F. Wyart, W.-Ü.L. Tchang-Brillet, and Y.N. Joshi. Phys. Scr. **71**, 589 (2005).
14. B.E. Lemoff, G.Y. Yin, C.L. Gordon, III, C.P.J. Barty, and S.E. Harris. J. Opt. Soc. Am. B, **13**, 180 (1996).
15. F. Callegari, M. Gallardo, M. Raineri, A.G. Trigueiros, and J.G. Reyna Almandos. J. Quant. Spectrosc. Radiat. Transfer, **73**, 13 (2002).
16. C. Biedermann, R. Radtke, J.-L. Schwob, P. Mandelbaum, R. Doron, T. Fuchs, and G. Fußmann. Phys. Scr. **T92**, 85 (2001).
17. E. Biémont. J. Phys. B, **30**, 4207 (1997).
18. M. McGeoch. Appl. Opt. **37**, 1651 (1998).
19. K. Bergmann, O. Rosier, W. Neff, and R. Lebert. Appl. Opt. **39**, 3833 (2000).
20. T. Krücken, K. Bergmann, L. Juschkin, and R. Lebert. J. Phys. D, **37**, 3213 (2004).
21. K. Bergmann, G. Schriever, O. Rosier, M. Müller, W. Neff, and R. Lebert. Appl. Opt. **38**, 5413 (1999).
22. M.A. Klosner and W.T. Silfvast. J. Opt. Soc. Am. B, **17**, 1279 (2000).
23. I. Krisch, P. Choi, J. Larour, M. Favre, J. Rous, and C. Leblanc. Contrib. Plasma Phys. **40**, 135 (2000).
24. T. Boboc, R. Bischoff, and H. Langhoff. J. Phys. D, **34**, 2512 (2001).
25. L. Juschkin1, A. Chuvatin, S.V. Zakharov, S. Ellwi1, and H.-J. Kunze. J. Phys. D, **35**, 219 (2002).
26. V.M. Borisov, A.V. Eltsov, A.S. Ivanov, Yu.B. Kiryukhin, O.B. Khristoforov, V.A. Mishchenko, A.V. Prokofiev, A.Yu. Vinokhodov, and V.A. Vodchits. J. Phys. D, **37**, 3254 (2004).
27. M.S. Safronova, W.R. Johnson, and U.I. Safronova. Phys. Rev. A, **53**, 4036 (1996).
28. U.I. Safronova, W.R. Johnson, and J. Albritton. Phys. Rev. A, **62**, 052505 (2000).
29. U.I. Safronova, W.R. Johnson, M.S. Safronova, and A. Derevianko. Phys. Scr. **59**, 286 (1999).
30. U.I. Safronova, C. Namba, I. Murakami, W.R. Johnson, and M.S. Safronova. Phys. Rev. A, **64**, 012517 (2001).
31. S.M. Hamasha, A.S. Shlyaptseva, and U.I. Safronova. Can. J. Phys. **82**, 331 (2004).
32. U. Safronova, A.S. Safronova, S.M. Hamasha, and P. Beiersdorfer. At. Data Nucl. Data Tables, **92**, 47 (2006).
33. U. Safronova, A.S. Safronova, and P. Beiersdorfer. J. Phys. B, **39**, 4491 (2006).
34. W.R. Johnson, S.A. Blundell, and J. Sapirstein. Phys. Rev. A, **37**, 2764 (1988).
35. G. O'Sullivan. J. Phys. B, **18**, L765 (1982).
36. K.T. Cheng and C. Froese Fischer. Phys. Rev. A, **28**, 2811 (1983).
37. M.H. Chen, K.T. Cheng, and W.R. Johnson. Phys. Rev. A, **47**, 3692 (1993).
38. Y.K. Kim, D.H. Baik, P. Indelicato, and J.P. Desclaux. Phys. Rev. A, **44**, 148 (1991).
39. S.A. Blundell. Phys. Rev. A, **47**, 1790 (1993).
40. L.D. Landau and E.M. Lifshitz. Quantum mechanics-non-relativistic theory. Pergamon Press, London. 1963. p. 281.
41. W.R. Johnson, D.R. Plante, and J. Sapirstein. Adv. At. Mol. Opt. Phys. **35**, 255 (1995).
42. U.I. Safronova. Mol. Phys. **98**, 1213 (2000).
43. http://das101.isan.troitsk.ru/cowan.htm.

© 2008 NRC Canada